Nanoscale

PAPER

View Article Online
View Journal | View Issue

Cite this: *Nanoscale*, 2025, **17**, 18709

Radiopaque poly(5-acrylamido-2,4,6-triiodoisophthalic acid)-based copolymers as theranostic carriers for image-guided drug delivery†

Kristyna Kolouchova, *[a] Nele Pien, [a] Fatma Nalan Cetin,[a] Zulfiya Cernochova, [b] Joeri Van Meerssche,[a] Miroslav Slouf, [b] Andrei-Alexandru-Antonio Bara, [a] Ondrej Groborz, [c,d] Martin Hruby [b] and Sandra Van Vlierberghe *[a]

Advancements in disease understanding have led to a shift towards personalized medicine, which has driven the development of an approach called theranostics. This approach combines diagnostics and therapy in one integrated system. Radiopaque biomaterials allow for non-invasive imaging using X-ray and computed tomography (CT). However, conventional contrast agents like gold nanoparticles are costly and are not well-suited for drug encapsulation. In this study, new block and statistical copolymers were synthesized using reversible addition-fragmentation chain-transfer (RAFT) polymerization comprising poly(*N*-isopropylacrylamide) (PNIPAM) and poly(5-acrylamido-2,4,6-triiodoisophthalic acid) (PAATIPA), designed to combine radiopacity with drug delivery capabilities. PAATIPA's high iodine content provides strong contrast in CT scans, while PNIPAM's thermoresponsiveness allows for self-assembly at higher temperatures. The anionic nature of PAATIPA allows the efficient encapsulation of the cationic small-molecule rhodamine 6G. The copolymers exhibited an enhanced encapsulation of cationic rhodamine 6G (>90% at 35 w/w% of rhodamine) and excellent biocompatibility, as demonstrated in cytotoxicity assays. This study emphasizes the potential of PAATIPA-based copolymer materials as multifunctional, radio-opaque and stimuli-responsive materials for theranostic applications.

Received 15th May 2025,
Accepted 18th July 2025

DOI: 10.1039/d5nr02033f

rsc.li/nanoscale

1. Introduction

Theranostics—a combination of "therapeutics" and "diagnostics"—refers to the integration of diagnostic and therapeutic functions within a single platform, enabling personalized and targeted treatment strategies. Medical imaging, a cornerstone of theranostics, relies on a variety of methods including radiology (*e.g.*, X-ray, computed tomography (CT)),[1] positron emission tomography (PET),[2] single-photon emission computed tomography (SPECT),[2] magnetic resonance imaging (MRI),[3] ultrasound,[4] *in vivo* fluorescence imaging or optical coherence tomography (OCT).[5] One of the most commonly used techniques, ^{1}H MRI has advantages such as unlimited penetration depth and non-invasiveness. Theranostic systems usually employ T_1-contrast agents, including paramagnetic species, which are mostly Gd^{III}-containing systems, or T_2-contrast agents, employing superparamagnetic iron oxide nanoparticles (SPIONs).[6] However, health risks are associated with the presence or accumulation of (super)paramagnetic metals in the body.[7,8] Another approach entails ^{19}F MRI, which has similar benefits as ^{1}H MRI, while also offering high contrast in images

[a]*Polymer Chemistry and Biomaterials Group, Centre of Macromolecular Chemistry, Department of Organic and Macromolecular Chemistry, Ghent University, Krijgslaan 281, S4-Bis, 9000 Ghent, Belgium. E-mail: Kristyna.Kolouchova@UGent.be, Sandra.VanVlierberghe@UGent.be*
[b]*Institute of Macromolecular Chemistry, Czech Academy of Sciences, Heyrovského sq. 2, Prague 6, 162 06, Czech Republic*
[c]*Institute of Biophysics and Informatics, Charles University, First Faculty of Medicine, Salmovská 1, 12000 Prague 2, Czech Republic*
[d]*Institute of Organic Chemistry and Biochemistry, Czech Academy of Sciences, Flemingovo sq. 2, Prague 6, 160 00, Czech Republic*

† Electronic supplementary information (ESI) available: 1D and 2D NMR spectra of all synthesized polymers; gel permeation chromatography (GPC) chromatograms; dynamic light scattering (DLS) data; additional transmission electron microscopy (TEM) micrographs; turbidimetry plots; evaluated radiopacities of polymer solutions and PBS; cell seeding images; ^{1}H NMR, GPC, and DLS data of the reference polymer; calculations of degree of polymerization (DP), number-average molecular weight (M_n), and PNIPAM/PAATIPA ratios; examples of cationic APIs; and statistical analysis data. See DOI: **https://doi.org/10.1039/d5nr02033f**

("hot-spot" imaging).[9–12] Nevertheless, this technique lacks suitable tracers and is yet to be introduced in medical practice. On the other hand, methods like *in vivo* fluorescence imaging or OCT provide no-background detection of the applied theranostic material, similarly to ^{19}F MRI. However, these methods exhibit limited penetration depth (1–3 mm in OCT[13] and *in vivo* fluorescence[14]), hampering their use.

Among these techniques, X-ray and CT imaging are the most convenient due to of their low cost and time requirements, wide availability, high resolution and unlimited penetration depth. Additionally, in case of X-ray and CT imaging, the patient is only exposed to low-dose X-rays (radiation dose for X-ray is approx. 0.001 mSv to 0.1 mSv, while for CT usually ranging between 1.5–10 mSv) which is associated with only a low health risk, unlike in PET/SPECT (over 20 mSv).[15] The most common contrast agents used for radiology are based on an insoluble barium sulfate gastrointestinal (GI) tract contrast agent and iodinated small aromatic molecules.[16] Other commonly studied contrast agents are gold nanoparticles,[1,16–18] and their combination with polymers, *e.g.*, gold nanoparticles encapsulated in polyethylene glycol (PEG).[19] Additionally, coated nanoparticles using inorganic compounds, such as bismuth(III) sulfide (Bi_2S_3),[20] have also been reported. Finally, a liposomal system has been developed, with liposomes entrapping diatrizoic acid salts (Renografin) being used to target the spleen passively.[21]

Nevertheless, in order to expand the diagnostic system toward theranostics, the polymeric systems must be able to self-assemble and encapsulate or carry an active pharmaceutical ingredient (API). These systems, also known as 'drug-delivery systems' (DDSs), can improve the pharmacodynamics and pharmacokinetics of drugs. To date, several radiopaque-based monomers have been described. A polymer system prepared *via* emulsion polymerization of an iodinated monomer (2-methacryloyloxyethyl-(2,3,5-triiodobenzoate), MAOETB), which could potentially be used for drug encapsulation, has been shown to achieve significantly enhanced visibility of lymph nodes, liver, kidney, and spleen in dogs.[22] Another radiopaque monomer, 3-(methacryloylamidoacetamido)-2,4,6-triiodobenzoic acid (MABA), has been used to create CT-traceable crosslinked hydrogels.[23]

Recently, we described radiopaque gelatin-based hydrogels and poly(ε-caprolactone)-based biomaterials incorporating poly(5-acrylamido-2,4,6-triiodoisophthalic acid) (PAATIPA), applied in tissue engineering.[24,25] In the current study, we extended our previous work by using the AATIPA monomer to synthesize both block and statistical copolymers, leveraging the hydrophilic nature and radiopacity of PAATIPA rendering it a promising candidate for the development of a drug delivery system, either as polymeric particle or to serve as injectable implant. In addition to its radiopaque properties, the carboxylic acid groups in AATIPA confer pH-responsiveness ($pK_a \approx 2.3$), enabling advanced drug delivery functionalities such as enhanced encapsulation of cationic drugs, complexation with cationic peptides, or accelerated release at elevated pH, characteristic of infected or inflamed tissues.[26]

To further enhance functionality, the polymers were herein combined with poly(*N*-isopropylacrylamide) (PNIPAM), a thermoresponsive polymer exhibiting a lower critical solution temperature (LCST) in aqueous environments. Below the LCST, PNIPAM-based polymers remained soluble, while heating above this threshold, induced phase separation and self-assembly. The architecture of the copolymers—block *versus* statistical—strongly influenced their self-assembly behaviour and potential applications. As have been previously described for other block copolymers, they could form well-defined nanostructures such as micelles or vesicles, making them suitable for drug encapsulation, nanomedicine, or tissue and cell labelling.[27–32] In contrast, statistical copolymers, although more compositionally disordered, could still exhibit LCST-driven thermoresponsiveness and are promising candidates to serve as injectable depots or as tissue labelling systems.[33,34] To comprehensively characterize the synthesized polymers, a range of analytical techniques was employed. Gel permeation chromatography (GPC) was used to assess molar mass distribution and dispersity. 1D and 2D NMR spectroscopy provided insights into polymer composition and structural integrity, while elemental analysis allowed quantification of iodine content, thereby confirming PAATIPA incorporation. Dynamic light scattering (DLS) was used to study the nanoparticle size and cloud point transitions (T_{CP}) of the block copolymers, and turbidimetry was employed to determine the LCST of the statistical copolymers. Transmission electron microscopy (TEM) was used to confirm the size and morphology of the nanoparticles. Drug encapsulation was tested using cationic rhodamine-6G and the cytotoxicity of the polymers was tested. The detectability of the materials was confirmed by μCT.

2. Experimental section

2.1. Materials

4-Cyano-4-[(dodecylsulfanylthiocarbonyl)sulfanyl]pentanoic acid (≥97%, CDPA), azobisisobutyronitrile (AIBN, ≥98%), 10 v/v% fetal bovine serum (FBS), rhodamine-6G, 2,6-di-*tert*-butyl-4-methylphenol (BHT), DMSO-*d*6, sodium phosphate monobasic ($NaH_2PO_4{\cdot}2H_2O$), sodium nitrate ($NaNO_3$), sodium azide (NaN_3), and *N*-isopropylacrylamide monomer were purchased from Sigma-Aldrich (Diegem, Belgium). Methanol (MeOH), tetrahydrofuran (THF) and *N*,*N*′-dicyclohexylcarbodiimide were purchased from Acros Organics (Geel, Belgium) and dried using conventional procedures before use. CD_3OD (methanol-d4, 99.80% D) was purchased from Eurisotop (Saint-Aubin, France). Gibco™ DMEM, high glucose (GlutaMAX™ Supplement, pyruvate), propidium iodide (PI), calcein-acetoxymethyl (Ca-AM), and 1 v/v% penicillin/streptomycin were purchased from ThermoFisher Scientific (Merelbeke-Melle, Belgium). 3-(4,5-Dimethylthiazol-2-yl)-5-(3-carboxymethoxyphenyl)-2-(4-sulfophenyl)-2*H*-tetrazolium (MTS) was purchased from Abcam (Amsterdam, Netherlands). Human foreskin fibroblast cells (HFF-1, SCRC-1041™) were purchased from ATCC (Glasgow, UK). 5-Amino-2,4,6-triiodoisophthalic acid

(ATIPA) and acrylic anhydride (stabilised with 10% 4-methoxyphenol) were purchased from Fluorochem (Derbyshire, UK) and stored in the freezer before use. Dimethylformamide (DMF, ≥99.0%), diethyl ether (DEE, ≥98%), and acetonitrile (MeCN, ≥99.0%) were purchased from TCI and dried over molecular sieves (4 Å) before use.

2.2. Methods

2.2.1. Synthesis of AATIPA monomer. The AATIPA monomer synthesis started with dispersing 18 g (0.032 mmol) of ATIPA in 120 mL of dry acetonitrile in a 250 mL two-neck round bottom flask equipped with a large magnetic stirring bar. Afterwards, a reflux condenser was attached, and the apparatus was flushed with argon for 15 min. Then, the dispersion was cooled down using ice bath and 35 μL of glacial sulfuric acid and acrylic anhydride (10 g, 0.08 mmol) were added dropwise to the mixture. A catalytic amount of BHT was added to avoid any polymerization. Following these steps, the mixture was heated to 80 °C and allowed to react for 48 h. Afterwards, the reaction mixture was cooled to room temperature, the product was filtered, washed with acetonitrile and dried in a desiccator for 2 days. A white powder product with a yield of 89% was obtained.

2.2.2. Synthesis of pNIPAM macro-CTA. PNIPAM-based macroCTAs and PAATIPA homopolymer were prepared *via* RAFT polymerisation, using CDPA as chain transfer agent (CTA) and AIBN as initiator, targeting two molar masses, 10 kg mol^{-1} and 20 kg mol^{-1}, as described earlier (Fig. 1).[39] The respective monomer (NIPAM or AATIPA), AIBN and CDPA were dissolved in DMF, and the mixtures were flushed with argon for 15 minutes. The reaction was conducted at 70 °C overnight under moderate stirring. The corresponding quantities of the starting materials are listed in Table 1. After the reaction, the polymers were precipitated in dry DEE, redissolved in ultrapure water, and freeze-dried to yield a yellowish powder. The PNIPAM polymers were then used as macromolecular chain transfer agents (macroCTAs) in the subsequent synthesis of diblock copolymers **B1–B6**.

2.2.3. Synthesis of PNIPAM-*b*-PAATIPA. Diblock PNIPAM-*b*-PAATIPA copolymers were prepared using the PNIPAM-based polymers as macroCTA (Fig. 1). From both **PNIPAM-1** and **PNIPAM-2, 3** different diblock copolymers were prepared targeting around 10 kg mol^{-1}, 20 kg mol^{-1} and 30 kg mol^{-1} for the theoretical molar mass of the pAATIPA block (theoretical target DPs between 11 and 55). The corresponding quantities of the starting materials are depicted in Table 2. The RAFT polymerization was performed similar to the synthesis of the PNIPAM-based macroCTA (*vide supra*). After the reaction, the polymers were precipitated in dry DEE, redissolved in ultrapure water, and dialyzed against ultrapure water for 24 h, using a dialysis membrane with a 1000 Da molar mass cut-off. After dialysis, the polymers were freeze-dried to obtain yellowish powders corresponding with polymers **S1–S6**, with yields listed in Table 2.

2.2.4. Synthesis of PNIPAM-*s*-PAATIPA. Statistical copolymers PNIPAM-*s*-PAATIPA were prepared *via* RAFT co-polymeriz-

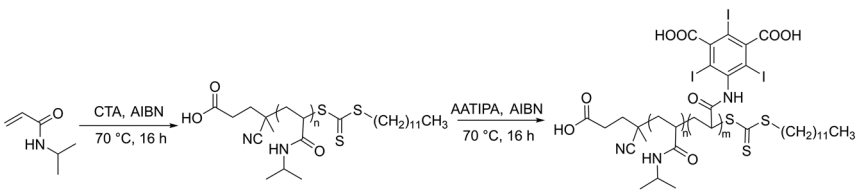

Fig. 1 Synthesis of PNIPAM and PNIPAM-*b*-PAATIPA block copolymers.

Table 1 Quantities of starting materials, targeted DPs and yields

Pol.	$m_{monomer}$ (g)	$n_{monomer}$ (mmol)	m_{AIBN} (mg)	n_{AIBN} (mmol)	m_{CDPA} (mg)	n_{CDPA} (mmol)	V_{DMF} (mL)	DP_{theor}	Yield (%)
PNIPAM 1	2.00	17.7	23.8	0.14	113	0.28	6.00	63	76.4
PNIPAM 2	2.00	17.7	11.8	0.07	56.6	0.14	6.00	126	78.2
PAATIPA	1.00	1.60	3.30	0.02	33.2	0.08	4.00	20	87.6

Table 2 Quantities of starting materials, targeted DPs and yields

Pol.	macro-CTA	m_{AATIPA} (mg)	n_{AATIPA} (mmol)	$m_{PNIPAM\text{-}CTA}$ (mg)	$n_{PNIPAM\text{-}CTA}$ (mmol)	m_{AIBN} (mg)	n_{AIBN} (mmol)	V_{DMF} (mL)	DP_{theor}	Yield (%)
B1	**PNIPAM 1**	245	0.39	400	0.02	2.50	0.02	1.30	17	62.6
B2	**PNIPAM 1**	245	0.39	200	0.01	1.20	0.007	0.90	34	57.4
B3	**PNIPAM 1**	368	0.59	200	0.01	1.20	0.007	0.90	51	67.8
B4	**PNIPAM 2**	245	0.39	400	0.01	2.50	0.02	1.30	26	62.9
B5	**PNIPAM 2**	245	0.39	200	0.007	1.20	0.007	0.90	53	63.6
B6	**PNIPAM 2**	367	0.59	200	0.007	1.20	0.007	0.90	80	60.9

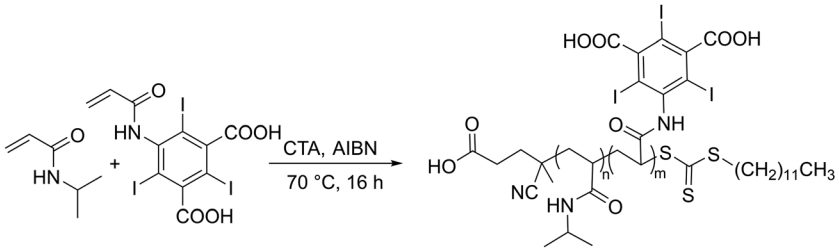

Fig. 2 Synthesis of PNIPAM-*s*-PAATIPA statistical copolymers.

ation, mixing NIPAM and AATIPA monomers, in the presence of CDPA as CTA, and AIBN as initiator (Fig. 2). The corresponding quantities of the starting materials are listed in Table 3. Furthermore, the RAFT polymerization conditions and purification of the resulting polymers was performed as described for the synthesis of PNIPAM-*b*-PAATIPA (*vide supra*), obtaining yellowish powders with yields listed in Table 3.

2.2.5. Size exclusion chromatography (SEC). M_w, M_n, and $Đ_M$ (M_w/M_n) of the obtained polymers were determined using two different SEC systems. The first system is an Agilent 1260-series HPLC system equipped with a 1260 ISO-pump, an automatic liquid sampler (1260), a column compartment heated to 50 °C equipped with two Plgel 5 μm mixed-D columns (Avantor® ScienceCentral, Tilburg, Netherlands) and a precolumn in series, a RI detector, along with a 1260 diode array detector (DAD). The eluent was DMAc containing 50 mM LiCl at a flow rate of 0.5 mL min^{-1}. Molar mass values and dispersities were calculated against PMMA standards. The chromatograms were analysed using Agilent GPC Data Analysis Software (Agilent Technologies, CA). To prepare samples for this system, the carboxylic acids of the AATIPA monomeric units were methylated using the following conditions: the polymer (50 mg) was dissolved in 1 mL of dry DMF to which one flake of KOH was added. The solution was stirred, 60 mL (approx. 1.5 eq. of carboxylic groups) of MeI was added and the reaction was left to stir for 2 h at room temperature. Afterwards, the polymers were purified *via* precipitation in DEE and dried. Additionally, all the PAATIPA-containing polymers were also measured using an anionic SEC system, constituting a Waters 410 differential refractometer, Waters photodiode array detector, Waters 600 controller with an isocratic pump, Waters 610 fluid control, Rheodyne injection unit with a 20 μL loop and two Shodex SB-806M HQ (OHpak) columns. A mobile phase consisting of an aqueous buffer containing 80 v/v% of phosphate-nitrate buffer (0.01 M $NaH_2PO_4{\cdot}2H_2O$ and 0.2 M $NaNO_3$ in ultrapure water at pH 7) and 20 v/v% of MeOH was used to run the samples. Each sample was dissolved at a concentration of 10 mg mL^{-1}. The calibration curve was obtained using monodisperse dextran standards (M_n = 4.3–202 kg mol^{-1}).

2.2.6. Synthesis of reference PEG-PNIPAM block copolymer. The reference polymer, PEG-PNIPAM, was synthesized by dissolving 300 mg (2.65 mmol) of NIPAM with 100 mg PEG-CTA (4.0 kg mol^{-1}, 0.025 mmol), as previously described,[35] in a Schlenk flask with 1.5 mL dry DMF. Afterwards, 138 μL of AIBN stock solution (1.6 mg ml^{-1}) was added to the solution and the final polymerization mixture was bubbled with argon for 15 min. The reaction was left to stir for 16 hours. After 16 hours, the polymer was precipitated in diethyl ether, redissolved in water and freeze-dried.

2.2.7. 1D and 2D NMR spectroscopy. The ^{1}H NMR, COSY, and HSQC spectra of the synthesized polymers were recorded using a Bruker Avance MSL 400 MHz spectrometer. The spectra were processed and analysed using the software MestReNova, version 12.0.0.

2.2.8. Dynamic light scattering (DLS). The cloud point temperature (T_{CP}) and the hydrodynamic radii (R_H) of self-assembled structures based on block copolymers **B1–B6** in aqueous solution were determined using a Zetasizer Nano-ZS Malvern apparatus (Malvern Instruments, Malvern, UK). The measurements were conducted under a controlled temperature ramp, spanning from 15.0 °C to 50.0 °C, with incremental increases of 1.0 °C. The instrument was equipped with a helium–neon (He–Ne) laser as the excitation source, emitting light at 633 nm. The scattered light intensity was measured at a backscatter angle of 173° and the solutions of the polymers

Table 3 Quantities of starting materials, targeted DPs and yields

Pol.	m_{NIPAM} (g)	n_{NIPAM} (mmol)	m_{AATIPA} (mg)	n_{AATIPA} (mmol)	m_{AIBN} (mg)	n_{AIBN} (mmol)	m_{CDPA} (mg)	n_{CDPA} (mmol)	V_{DMF} (mL)	DP_{theor}	Yield (%)
S1	1.90	16.8	100	0.16	2.50	0.015	56.5	0.1400	1.30	121	76.00
S2	1.80	15.9	200	0.32	1.20	0.007	56.5	0.1400	0.90	116	71.05
S3	1.70	15.0	300	0.48	1.20	0.007	56.5	0.1400	0.90	111	57.15
S4	1.60	14.1	400	0.64	2.50	0.015	56.5	0.1400	1.30	106	34.05
S5	1.50	13.3	500	0.80	1.20	0.007	56.5	0.1400	0.90	100	44.60
S6	1.00	8.84	100	0.16	1.20	0.007	56.5	0.1400	0.90	64	44.00

were prepared in phosphate-buffered saline (PBS) at a concentration of 1 mg mL^{-1}. The data were processed with the Repes algorithm as well as Zetasizer software.[36] The zeta potentials were measured using a Zetasizer NanoZS instrument (model ZEN3600 from Malvern Instruments, UK) at temperatures of 37 °C. A scattering angle of $\theta = 13°$ was used, and the data was processed with Malvern software. The zeta potential data was evaluated using the Smoluchowski model.

2.2.9. Transmission electron microscopy (TEM). The morphology of the nanoparticles was visualized using a TEM microscope (Tecnai G2 Spirit Twin 12; FEI Company, Brno, Czech Republic). The selected polymers **B1** and **B4** were characterized at a polymer concentration of 1.0 mg mL^{-1} in water after applying the previously reported fast-solvent-removal protocol and negative staining with uranyl acetate.[37] For both samples, the fast solvent removal was performed at room temperature (22 °C) and at elevated temperature above the LCST (50 °C). This enabled the observation of the fixed morphology of each sample above and below the LCST, as described elsewhere.[37] Briefly, the fast solvent removal followed by negative staining was performed as follows: 2.0 μL of the solution was deposited on a carbon-coated copper TEM grid and left to evaporate for 1 min. Subsequently, the excess of solvent on the grid was removed by touching the bottom of the grid with a small piece of filter paper. This fast removal of the solution minimizes drying artifacts, as shown in our previous studies.[37] The dried sample was negatively stained with uranyl acetate: 2 wt% aqueous solution of UO_2Ac_2 was dropped on the dried specimen from the previous step, left to equilibrate for 1 min, and the excess of UO_2Ac_2 solution was removed by touching the bottom of the grid with filter paper, similar as in the previous step. The dried samples were equilibrated for at least 1 hour in air at room temperature and then they were observed in TEM using bright field imaging at 120 kV. The fast solvent removal at 50 °C was performed in the same way as described above, but all solutions (polymer and UO_2Ac_2) and preparation tools (tweezers, microscopic grids, *etc.*) were incubated in an oven at 50 °C for 15 min before sample preparation. The polymer solution deposition was performed outside the oven, but all evaporations and equilibrations took place in the oven heated at 50 °C.

2.2.10. Turbidimetry. The lower critical solution temperatures (LCSTs) of the statistical copolymers **S1** and **S2** were determined by turbidimetry using Cristyal 16 parallel crystallizer turbidimeter (Avantium Technologies, Ontario, Canada) coupled with a recirculation chiller. Aqueous solutions of the polymers were prepared in 140 mM PBS, at pH of 7.4. Polymer solutions were prepared at five distinct concentrations: 10, 25, 50, and 100 mg mL^{-1}. First, the polymer solutions were equilibrated at 10.0 °C, followed by a heating cycle to 80.0 °C at a 0.5 °C min^{-1} rate. Afterwards, the samples were cooled down to 10.0 °C and equilibrated for 30 min. This process was repeated in 6 consecutive cycles. Turbidity was monitored throughout using 600 nm light transmission, with stirring at 700 rpm to ensure a uniform heat distribution.

2.2.11. Elemental analysis. Elemental analysis was performed to determine the composition of the synthesized polymers. The C/H/N composition of freeze-dried hydrogels was measured using PE 2400 Series II CHNS/O analyzer (PerkinElmer, USA) in combustion mode (pure oxygen). The mass of all samples was 1.5 ± 0.1 mg (all samples were weighted with a calibrated scale with an accuracy of 0.001 mg). The absolute uncertainty of CHN determination is ≤0.3 abs%. The instrument was calibrated before use. All samples were measured in two independent experiments. The iodine content was determined using X-ray Fluorescence Spectrometer SPECTRO Xepos P (AMETEK Materials Analysis Division, Zábřeh, Czechia).

2.2.12. Determination of pK_a. The pK_a value of PAATIPA was determined using a voltametric/electrochemical pH detector, a reliable method for assessing the acid dissociation properties of the polymer in an aqueous environment. The experimental protocol commenced with the dissolution of 10 mg of PAATIPA in 1.0 mL of ultrapure water, ensuring a homogeneous solution free from impurities that might interfere with the measurement. This was followed by the stepwise addition of 30 μL increments of 0.1 M NaOH, a process carefully designed to allow precise monitoring of the polymer's response to changes in pH. The pK_a value was calculated using a graphical method, where the data collected during the titration were analysed to pinpoint the inflection point corresponding to the deprotonation of the functional groups in PAATIPA.

2.2.13. Micro-computed tomography (μCT). μCT images were acquired with a preclinical X-CUBE micro-CT system (MOLECUBES; Ghent, Belgium), in "General-purpose mode" as previously described.[38] This mode encompassed a continuous scan, tube voltage of 50 kV, tube current of 75 μA, 480 projections (each projection has 1 averaging), acquisition per projection 125 ms, total acquisition time 90 s, dose per one bed position 18 mGy. The X-ray source (X-ray tube) was a fixed tungsten anode with a 0.8 mm aluminium filter and a non-variable focal spot size of 33 μm. The flat-panel detector was based on CMOS technology (14-bits) using a CsI scintillator. It consists of 1536 × 864 pixels for an active area of 115 mm × 65 mm with a pixel size of 75 μm. Further hardware and software details are described in previous work.[38]

2.2.14. Drug loading. A stock solution of rhodamine 6G (3.5 mg mL^{-1}) was prepared, from which serial dilutions were obtained using ultrapure water to obtain final concentrations of 2.0 mg mL^{-1}, 1.0 mg mL^{-1} and 0.5 mg mL^{-1}. To each solution, 10 mg of polymer was added, and the resulting polymer-rhodamine solutions were transferred to Amicon® Ultra Centrifugal Filter, 30 kDa MWCO (Sigma-Aldrich, Diegem, Belgium). A sample of the solution was taken and diluted 1 : 100 with DMSO. Afterwards, the solutions were centrifuged at 11 000 rpm for 10 minutes in a preheated centrifuge to 37 °C. After centrifugation, samples of the filtrate were collected and diluted 1 : 100 with DMSO. Absorbance measurements were conducted using the UV-

plate reader and a Greiner 96-flat transparent well plate with the wavelength set at the absorbance maximum (540 nm). The absorbance values were used to quantify the mass of rhodamine m_{Rhod} in both the initial solution and in the filtrate ($m_{\mathrm{Rhod,\ initial}}$ and $m_{\mathrm{Rhod,\ filtr}}$, respectively). Encapsulation efficiency and drug loading were subsequently calculated using eqn (1) and (2).

$$\mathrm{EE}\,(\%) = \frac{m_{\mathrm{Rhod,\,initial}} - m_{\mathrm{Rhod,\,filtr}}}{m_{\mathrm{Rhod,\,filtr}}} \times 100 \quad (1)$$

$$\mathrm{DL}\,(\%) = \frac{m_{\mathrm{Rhod,\,initial}} - m_{\mathrm{Rhod,\,filtr}}}{m_{\mathrm{polymer}}} \times 100 \quad (2)$$

2.2.15. Cytotoxicity assay. Human foreskin fibroblasts (HFFs) were maintained at 37 °C in a humidified atmosphere in the presence of 5% CO_2. Cells were cultured in high-glucose DMEM supplemented with 10% (v/v) FBS, 1% (v/v) penicillin/streptomycin (P/S), GlutaMAX™ and sodium pyruvate. The medium was refreshed twice weekly until cells reached 80–90% confluency. Passage 3 HFFs were used for all experiments and seeded at a density of 10 000 cells per well in 96-well plates. Studied polymers with the highest PAATIPA content (**B3**, **B6**, **S5**, and **S6**) were sterilized through 2 times 2 h of UV-C irradiation (before and after weighing the samples, 100 to 280 nm, 15 mW cm^{-2}). Afterwards, the polymers were dissolved in medium, to obtain polymer concentrations of 2.0, 1.0, and 0.5 mg mL^{-1} and the resulting solutions were further sterilized by sterile filtration.

Cell viability was assessed on days 1, 3, and 7 post-seeding using a calcein-AM/propidium iodide (Ca-AM/PI) live/dead staining method (n = 3). At each time point, the medium was replaced with 100 μL of staining solution containing 2% (v/v) Ca-AM and 2% (v/v) PI in DPBS. After 15 minutes of incubation at room temperature in the dark, fluorescence images were acquired using a Zeiss LSM710 confocal microscope with a 10×/0.25 air objective, using GFP and Texas Red channels. ImageJ was used to quantify the amount of living and dead cells, and the viability was calculated according to the following eqn (3):

$$\mathrm{Viability}\,(\%) = \frac{\#\mathrm{living\ cells}}{\#\mathrm{living\ cells} + \#\ \mathrm{dead\ cells}} \times 100\,. \quad (3)$$

Metabolic activity was measured using an 3-(4,5-dimethylthiazol-2-yl)-5-(3-carboxy-methoxyphenyl)-2-(4-sulfophenyl)-2*H*-tetrazolium (MTS) assay (n = 3 per time point). On days 1, 3, and 7, the culture medium was removed and replaced with fresh DMEM (without supplements) containing 10% (v/v) MTS reagent. After 2 hours of incubation at 37 °C in the dark, the absorbance was measured at 490 nm using a Tecan Infinite M200 Pro microplate reader. Background absorbance (media with MTS but without cells) was subtracted from all readings. Data were normalized to the absorbance of control cells on day 1 (set as 100%).

3. Study design

The aim of this study was to evaluate the feasibility of developing block and statistical copolymers incorporating poly(5-acrylamido-2,4,6-triiodoisophthalic acid) (PAATIPA), a hydrophilic and radiopaque polymer, for the formation of self-assembled nanoparticles suitable for drug delivery. Poly(ethylene glycol) (PEG) is a commonly used hydrophilic polymer block that has increasingly been associated with allergenic reactions, including rare cases of anaphylactic shock.[39] Due to the widespread use of PEG-based detergents as well as PEG-coated nanovaccines, an increasing number of people in Western populations have developed anti-PEG antibodies. In fact, a recent study of plasma samples from hospitals and service providers in the United States detected antibodies in 65–76% of the samples.[40] As a result, alternative materials are being explored.[41] PAATIPA presents a promising alternative to PEG. Importantly, PAATIPA confers intrinsic radiopacity, enabling *in vivo* detection without the need for external contrast agents.

To assess the suitability of PAATIPA for self-assembling systems, a PAATIPA homopolymer and twelve PAATIPA-PNIPAM copolymers—six block copolymers and six statistical copolymers were synthesized. Incorporation of poly(*N*-isopropylacrylamide) (PNIPAM) imparts thermoresponsive behavior to the copolymers, characterized by a lower critical solution temperature (LCST). As previously demonstrated for related systems, heating aqueous solutions of such copolymers above their cloud point temperature (T_{CP}) triggers self-assembly into well-defined nanoparticles or injectable polymeric materials, depending on the polymer architecture. Block copolymers, due to their propensity to form micelles and other nanostructures, are well suited for drug delivery applications[42] whereas statistical copolymers may be advantageous for forming injectable materials for sustained release or tissue labeling.[33,34] Hence, both copolymer architectures offer complementary functions depending on the therapeutic application.

Furthermore, the polyanionic nature of PAATIPA may enhance the encapsulation efficiency of cationic drugs or facilitate complexation with positively charged peptides. All synthesized polymers were systematically characterized to determine their chemical structure, molar mass distribution, composition, and thermoresponsive properties.

4. Results and discussion

4.1. PNIPAM-*b*-PAATIPA diblock copolymers

4.1.1. Synthesis and characterization of PNIPAM-*b*-PAATIPA diblock copolymers. To prepare the block copolymers, two PNIPAM macro-chain transfer agents (macroCTAs) were first synthesized *via* RAFT polymerization, targeting different degrees of polymerization (DPs). The resulting macroCTAs exhibited narrow molar mass distributions, as confirmed by size exclusion chromatography (SEC) (Table 4), indicating good control over the polymerization process. The successful synthesis and purity of PNIPAM were verified by ^{1}H,

Table 4 Characterization of the resulting PNIPAM and PNIPAM-*b*-PAATIPA copolymers. M_n, M_w, $Đ_M$, targeted and resulting DP of PAATIPA calculated from SEC (DMAc) or elemental analysis, iodine and AATIPA content in the resulting block copolymers calculated from elemental analysis, calculated M_n of the resulting polymer using the obtained DP from elemental analysis

Pol.	DP_{teor}	M_n [b] (kg mol^{-1})	M_w [b] (kg mol^{-1})	$Đ_M$ [b]	PAATIPA[a] (wt%, EA)	DP	M_n [a] (EA, kg mol^{-1})	I[a] (wt%)
PNIPAM1	63	17.4	19.1	1.09	0.00	153[b]	N/A	0.00
PNIPAM2	126	27.3	30.2	1.11	0.00	238[b]	N/A	0.00
B1	80	16.4	20.4	1.24	26.8	74[a]	24.2	16.4
B2	97	15.1	20.2	1.34	50.1	93[a]	36.0	30.7
B3	114	19.4	22.2	1.44	58.2	105[a]	43.5	35.6
B4	152	26.5	33.0	1.25	26.5	143[a]	37.9	16.2
B5	179	22.5	30.7	1.37	40.8	159[a]	47.8	25.0
B6	206	26.0	32.9	1.27	45.4	166[a]	52.1	27.8

[a] Determined *via* SEC and elemental analysis. [b] Determined *via* SEC.

COSY and HSQC NMR spectroscopy (Fig. S4–S9†), which showed the expected resonances for the isopropyl side group and the polymer backbone.

Using the two PNIPAM macroCTAs, a series of six diblock copolymers, **B1–B6**, were synthesized with varying target DPs for the PAATIPA block. The presence of the PAATIPA segment was confirmed by NMR spectroscopy (Fig. S10–S27 and Table S1†). While ^{1}H NMR spectroscopy enabled qualitative confirmation and approximate estimation of the PAATIPA content in the diblock copolymers, the quantitative accuracy was limited due to overlapping signals and differing relaxation behaviours of the PNIPAM and PAATIPA segments. Therefore, the iodine content was determined *via* elemental analysis to more precisely quantify the degree of AATIPA incorporation. The values obtained from the elemental analysis were used to calculate the DP of the PAATIPA block and the overall molar mass of the copolymers, based on the experimentally determined M_w of the PNIPAM segment. A detailed description of these calculations is provided in section S7 of the ESI.†

SEC was used to assess the molar mass and dispersity ($Đ_M$) of the copolymers. Initial measurements in aqueous SEC conditions, optimized for polyanionic polymers, yielded molar masses that were significantly lower than expected (Table S2 and Fig. S61†). In fact, the observed polymer lengths were shorter than those of the PNIPAM macroCTAs, indicating that the aqueous system was not well suited for the analysis of these block copolymers. Nevertheless, a trend of increasing molar mass from **B1** to **B6** was clearly observed (Table S2 and Fig. S61†). To overcome this issue, the carboxylic acid groups in PAATIPA were methylated using methyl iodide, rendering the polymer compatible with organic phase (DMAc) SEC. Under these conditions, the molar mass of the copolymers were more consistent with the theoretical values, although systematic underestimation due to structural differences from PMMA cannot be ruled out (Table 4 and Fig. S60†).

4.1.2. PNIPAM-*b*-PAATIPA diblock copolymer-based nanoparticles. As these polymers are designed to self-assemble upon heating above their cloud point temperature (T_{CP}), their hydrodynamic radii (R_h) as a function of temperature (15–50 °C) were monitored using dynamic light scattering (DLS) (Fig. 3 and Fig. S64–S71†). The key reference points were well below the T_{CP} (15 °C) and physiological temperature (37 °C).

Minor variations in T_{CP} were observed among the copolymers and were attributed to differences in block composition. Specifically, a higher PNIPAM content led to a lower T_{CP}, while a higher PAATIPA content resulted in increased T_{CP} values—consistent with PAATIPA's hydrophilicity. At 15 °C, well below the T_{CP}, the polymers remained in a molecularly dissolved state, exhibiting R_h values of approximately 3–4 nm (Table 5). These values correspond with unimers, although DLS also detected a minor population of larger particles (~30 nm), which are likely an artifact due to light scattering bias: DLS is disproportionately sensitive to larger particles due to their higher scattering intensity, and the negligible abundance of these particles at low temperatures is supported by volume- and number-based DLS distributions (Fig. S72–S77†).

Upon heating above the T_{CP} (around 30–35 °C), the unimers undergo temperature-triggered self-assembly into significantly larger nanostructures, with R_h values ranging from 100 to 1000 nm (Table 5). In some samples, traces of even larger aggregates were also observed (Fig. 3 and S64–S71†), however, due to the above mentioned disproportionally higher scattering intensity for larger aggregates, these aggregates appear negligible when viewed in volume- or number-based distribution plots (Fig. S72–S77†). Furthermore, in case of polymer **B5**, where larger aggregates with $R_h \sim 5000$ can be visible in volume-based distribution, while showing negligible contribution in the number-based distribution (Fig. S77†). Interestingly, at temperatures above 43 °C, selected samples (**B4**, **B5**, and **B6**) exhibited a secondary transformation, characterized by a decrease in R_h (Fig. 3 and Table 5). This behaviour may reflect thermal disaggregation or structural rearrangement of previously formed aggregates. It should be noted that polyanionic polymers often exhibit artificially high R_h values in DLS measurements, due to the presence of a diffuse electric double layer (DEL), which increases the apparent particle size.[43] Therefore, the measured R_h values may overestimate the actual physical dimensions of the particles.

Additionally, the zeta potential of the formed nanoparticles at 37 °C was evaluated (Table 5). The values ranged between −16 and −25 mV, with no statistically significant differences

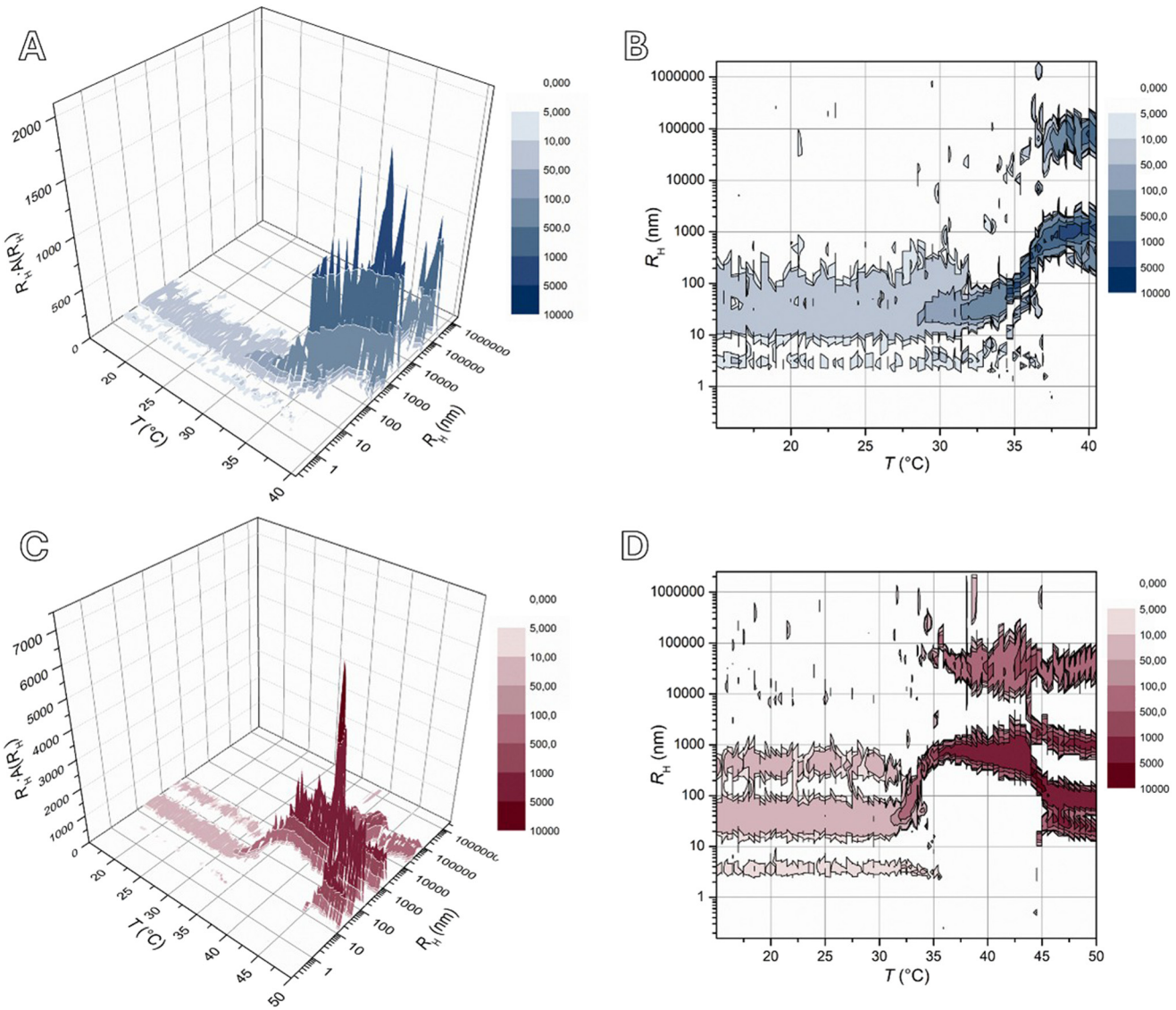

Fig. 3 Temperature dependence of self-assembly of (A and B) **B1** and (C and D) **B4** in PBS measured *via* DLS. In the graphs, we use equal-area representation: the vertical axis shows $R_h \cdot A(R_h)$, where $A(R_h)$ is the intensity distribution function of hydrodynamic radii R_h of particles in the sample.

Table 5 Evaluated data from DLS. T_{CP} corresponds to the temperature point at which self-assembly occurs, and in case of polymers **B4–B6**, also to the change in particle size

Pol.	T_{CP}		$R_H \pm$ SD (15 °C, nm)	$R_H \pm$ SD (15 °C, nm)	$R_H \pm$ SD (37 °C, nm)	$R_H \pm$ SD (45 °C, nm)		ZP (mV)
B1	34.5		3.1 ± 0.2	29 ± 15	87 ± 3	—		−16.4 ± 2.8
B2	35.4		3 ± 0.2	27 ± 9	618 ± 119	—		−23.8 ± 6.1
B3	35.5		3 ± 0.6	34 ± 14	138 ± 2	—		−18.4 ± 4.9
B4	34.4	43.5	4 ± 2	40 ± 7	819 ± 24	19 ± 7	151 ± 14	−22.1 ± 8.6
B5	33.9	43.5	4 ± 1	37 ± 8	250 ± 9	61 ± 8	131 ± 9	−29.7 ± 7.9
B6	30.9	42.5	4 ± 0.5	24 ± 13	1327 ± 67	50 ± 10	202 ± 47	−25.5 ± 5.9

between the samples ($p > 0.05$). This suggests an ionization of carboxylic acid groups on the nanoparticle surface, which is indicative of hydrophilic character and is relevant for biomedical applications, allowing for potential extended circulation time *in vivo*.[44] Such prolonged circulation could allow greater potential for tissue accumulation, especially when used in conjunction with active targeting strategies.

TEM was employed to examine the morphology and size of the nanoparticles and to further assess the potential influence of the diffuse electric double layer (DEL) on the hydrodynamic

radius measurements (Fig. 4, Fig. S78–S81†). At room temperature, representative samples **B1** and **B4**, primarily consisted of unimers with a small population of nanoparticles. The observed particle radii were 21 ± 3 nm for **B1** and 18 ± 6 nm for **B4**, aligning well with the hydrodynamic radii measured using DLS.

Following incubation at elevated temperature (50 °C), both samples underwent thermally induced self-assembly into well-defined nanoparticles. The average diameters increased to 77 ± 14 nm (**B1**) and 44 ± 7 nm (**B4**), confirming the temperature-triggered aggregation behaviour. The discrepancy between the nanoparticle sizes observed in TEM and the larger hydrodynamic radii measured *via* DLS likely arises from two factors: particle aggregation and the DEL effect, which inflates R_h values in aqueous media due to electrostatic repulsion and hydration layers. Importantly, TEM confirmed that PAATIPA-*b*-PNIPAM copolymers self-assemble into nanoparticles within the physiological temperature range. The resulting particles are consistently situated within the 20–500 nm size window—an optimal range for systemic drug delivery or tissue labelling applications.[42,45,46]

4.1.3. Encapsulation of cationic rhodamine 6G in PNIPAM-*b*-PAATIPA diblock copolymers. Self-assembled micelle-type

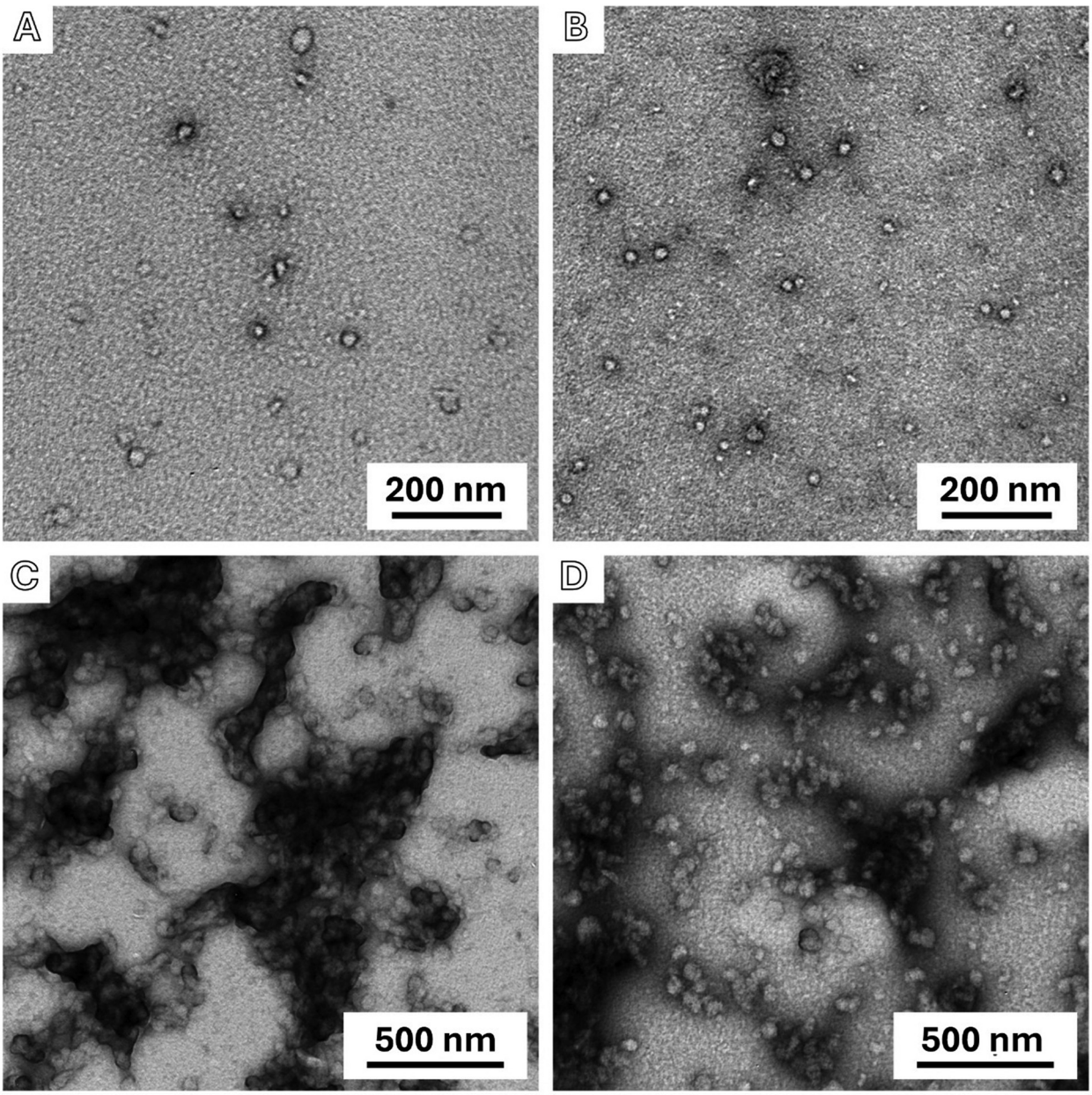

Fig. 4 TEM micrographs of polymer nanoparticles prepared by the fast-drying method combined with a negative staining using UO_2Ac_2. (A) **B1** and (B) **B4** samples were incubated at room temperature prior to drying. (C) **B1** and (D) **B4** samples were incubated in the oven at 50 °C prior to fast drying. The particle size was evaluated with ImageJ software (N = 8).

nanoparticles are promising candidates for the delivery of hydrophobic drugs.[42,45,46] However, as PNIPAM-*b*-PAATIPA copolymers form well-defined anionic particles, they are uniquely positioned to serve as drug delivery systems for both hydrophobic drugs (encapsulated within the thermoresponsive hydrophobic core) and hydrophilic cationic drugs (entrapped within the hydrophilic anionic corona), or cationic amphiphiles. To assess these properties, rhodamine 6G was used as a model of a small, partly hydrophilic, cationic drug, which has previously been described as effective for photodynamic therapy applications.[47]

At high rhodamine concentrations (3.5 mg of rhodamine per 10 mg of polymer, corresponding to 35 w/w%), PNIPAM-*b*-PAATIPA copolymers demonstrated exceptionally high encapsulation efficiencies (EE) of over 75% (Fig. 5), while at a lower drug concentration (10 w/w%), EE increased to over 90%. Notably, a trend emerged where copolymers with higher PAATIPA content exhibited a higher EE. Most significantly, polymer **B3**, with the highest PAATIPA/PNIPAM ratio, achieved the highest EE (>90%) at the highest rhodamine concentration. The corresponding drug loading (DL) values are presented alongside EE in Fig. 5.

To confirm the enhanced encapsulation effect due to the anionic PAATIPA, a reference polymer, PEG-PNIPAM was synthesized, and its EE and DL were evaluated (Fig. 5). The ^{1}H NMR, SEC and DLS evaluation of the PEG-PNIPAM reference polymer can be seen in Fig. S16–S18.† In contrast with PAATIPA-containing polymers, PEG-PNIPAM displayed much lower encapsulation efficiency (9% at 10 w/w% rhodamine concentration). These results underscore the potential of PAATIPA copolymers as effective hydrophilic blocks in self-assembled nanoparticles for drug delivery systems. Unlike conventional nanoparticles, which primarily deliver hydrophobic drugs, PAATIPA copolymers could also potentially enable the transport or local delivery of both hydrophilic cationic drugs or peptides, such as doxorubicin, lidocaine, insulin and tobramycin. Due to the aromatic nature of PAATIPA, additional interactions (*e.g.*, π–π stacking) may occur between PAATIPA and aromatic compounds such as rhodamine contributing to increased loading. Additional examples of potential drug candidates and their biomedical applications are listed in Tables S6 and S7.†

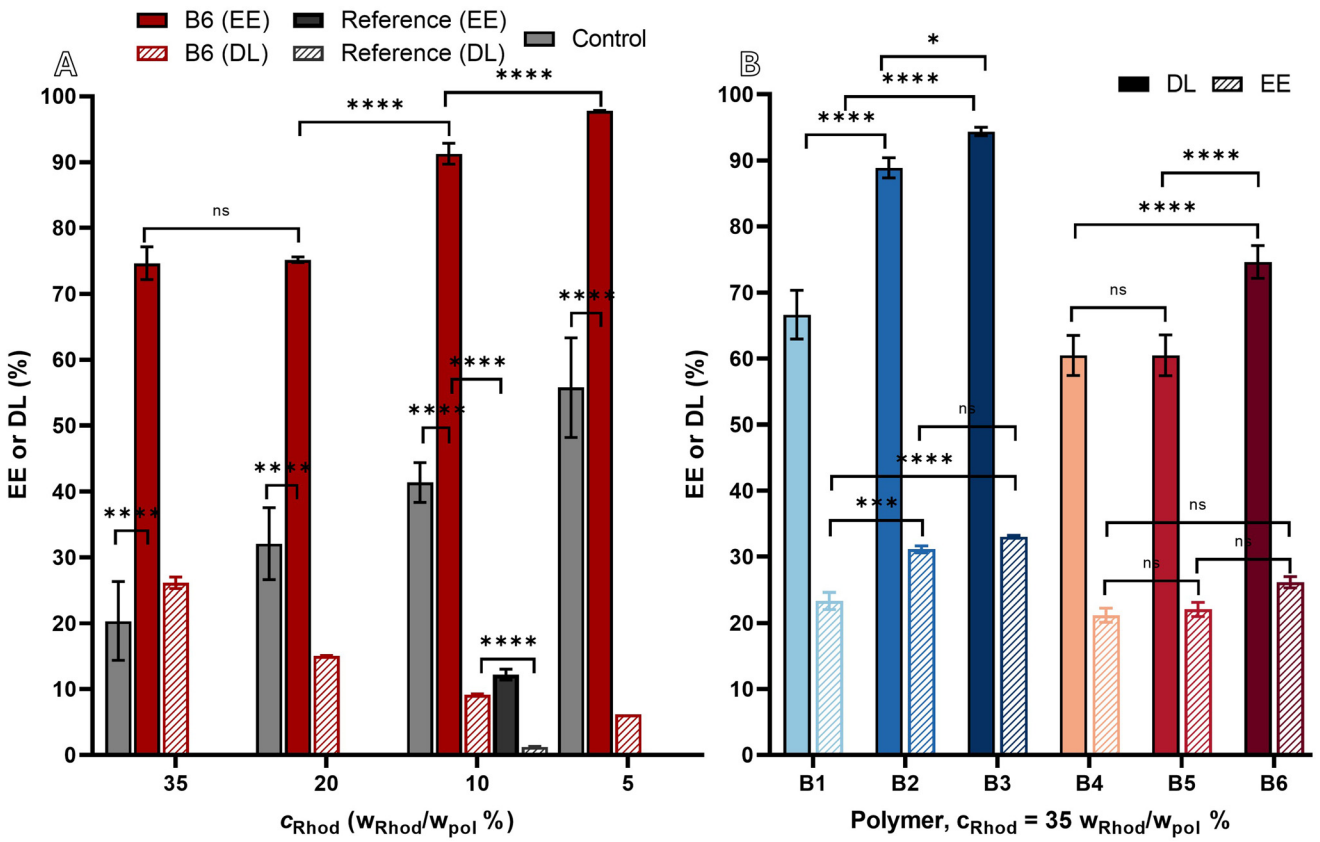

Fig. 5 Evaluated results from drug encapsulation assay. (A) DL and EE were evaluated for 4 different concentrations of rhodamine 6G (0.5, 1.0, 2.0 and 3.5 mg of rhodamine per 10 mg of polymer, depicted as c_{Rhod} of 5, 10, 20, and 35 w/w%, respectively) with polymer **B6**. (B) DL and EE were evaluated for the highest rhodamine 6G concentration (c_{Rhod} of 35 w/w%) with all block copolymers **B1–B6**. All experiments were performed in triplicate (N = 3), and statistical analysis was conducted using one-way ANOVA in GraphPad Prism version 8.4.3. Asterisks indicate levels of statistical significance: p < 0.05 (*), p < 0.01 (**), p < 0.001 (***), and p < 0.0001 (****); "ns" indicates no significant difference. For more detailed data analysis, see section S8 in ESI.†

4.2. PNIPAM-*s*-PAATIPA statistical copolymers

Six different statistical copolymers of PAATIPA-*s*-PNIPAM were synthesized and characterized using two different SEC systems (Fig. S62 and S63†), ^{1}H NMR spectroscopy (Fig. S28–S45†), and elemental analysis. The yields, molar masses (M_w, M_n), polydispersities ($Đ_M$), iodine content, theoretical and experimental DPs (calculated from DMAc SEC) and AATIPA content (evaluated by elemental analysis) are provided in Table 6. The AATIPA content of the statistical polymers, obtained *via* ^{1}H NMR spectroscopy, was similar to that of the diblock copolymers (Table S1†). However, elemental analysis provided a more accurate and reliable quantification of the actual AATIPA content in both the statistical and the block copolymers (Table 6).

4.2.1. Thermoresponsiveness of statistical copolymers. To evaluate the lower critical solution temperature (LCST) behavior of the synthesized statistical copolymers, T_{CP}s were measured *via* turbidimetry over the temperature range of 10–80 °C (Table 7 and Fig. S82–S107†). The T_{CP}s of the statistical copolymers of PNIPAAM shift in the presence of comonomers, *i.e.* increase upon addition of hydrophilic comonomers and decrease upon incorporation of hydrophobic ones.[48] As expected, increasing the PAATIPA content increased the T_{CP} of the polymers. Only copolymers with low PAATIPA content (<20%; **S1–S4**) exhibited T_{CP}s values. Interestingly, some polymers displayed thermoresponsive behaviour only at higher concentrations (>50 mg mL^{-1}, >8.33 wt%), and overall turbidity decreased upon dilution, complicating the accurate determination of T_{CP} values at lower concentrations (Fig. 6 and Fig. S82–S107†). For copolymers **S1–S3**, the LCST was determined at 200 mg mL^{-1} (16.7 wt%) with values ranging between 33.1 and 34.4 °C, suggesting that these polymers may become insoluble at body temperature (37 °C). Conversely, **S4** exhibited a higher LCST of 40.5 °C, indicating solubility retention under physiological conditions.

To introduce additional tunability of the LCST, the carboxylic acid groups of PAATIPA were methylated—an approach previously used for organic phase SEC compatibility. The methylation modification yielded the corresponding methylated derivatives, **S1m–S6m**, containing poly(bis-methyl-5-acrylamido-2,4,6-triiodoisophthate) (PMAATIPA). The methylated polymers were characterized by 1D and 2D ^{1}H NMR spectroscopy (Fig. S108–S111†). To validate the expected reduction in hydrophilicity, the T_{CP} values of the methylated polymers were assessed at a polymer concentration of 10 mg mL^{-1} (1.04 wt%, Table 7), revealing significantly lowered LCSTs of 26.3, 22.8, 19.8 and 17.6 °C for **S1m–S4m**, respectively. Notably, polymers **S5m** and **S6m** became insoluble in water, further confirming the hydrophobic nature of the methylated PAATIPA units. The carboxylic acid methyl ester is significantly more hydrophobic than carboxylate, as the latter also involves interchain repulsive coulombic interactions that contribute to solubilization.

As mentioned earlier, the T_{CP} and hydrophilicity of the polymers directly affect the properties of injectable depots. A previous study[34] showed that polymers with a T_{CP} below body temperature form depots at the site of administration and do not migrate to remote organs such as kidneys and liver. Kolouchova *et al.*[33] have demonstrated that incorporating hydrophilic comonomers into these intramuscularly adminis-

Table 6 Characterization of the resulting PNIPAM, and PNIPAM-*b*-PAATIPA copolymers. M_n, M_w, $Đ_M$, and yields, targeted and resulting DP of PAATIPA calculated from SEC or elemental analysis; iodine and AATIPA content in the resulting block copolymers calculated from elemental analysis

Pol.	DP_{theor}	$DP^{a,b}$	PAATIPA[a] (wt%, EA)	M_n [b] (kg mol^{-1})	M_w [b] (kg mol^{-1})	$Đ_M$ [b]	I^a (wt%)
S1	123	227	3.96	26.5	28.1	1.06	2.46
S2	116	242	8.25	29.3	31.8	1.09	5.13
S3	109	210	12.2	26.3	28.1	1.06	7.61
S4	102	196	16.9	25.7	28.0	1.09	10.5
S5	95	195	19.4	26.2	28.9	1.10	12.5
S6	69	139	38.7	23.0	25.3	1.10	23.7

[a] Determined by elemental analysis. [b] Determined by SEC.

Table 7 T_{CP}s for polymers **S1–S6** and concentration ranges from 1.04 to 16.7 wt%, measured in 6 heating cycles. Samples **S1m–S4m** were measured in 3 cycles. **S4m** aggregates remained insoluble after a single cycle. **S5m** was not soluble in aqueous solutions

Polymer		T_{CP} (°C)						
c_{pol} (wt %)	PAATIPA (wt%)	16.7	8.33	4.17	2.08	1.04	c_{pol} (wt %)	1.04
S1	5	33.1 ± 0.28	39.3 ± 0.52	38.0 ± 0.55	40.6 ± 0.20	43.9 ± 0.18	**S1m**	26.3 ± 0.31
S2	10	34.9 ± 1.19	37.2 ± 1.27	39.7 ± 0.41	>80	>80	**S2m**	22.8 ± 0.83
S3	15	34.4 ± 0.21	36.6 ± 0.29	38.5 ± 1.17	42.6 ± 0.65	>80	**S3m**	19.8 ± 0.36
S4	20	40.5 ± 4.35	40.8 ± 0.48	45.0 ± 2.41	N/D	>80	**S4m**	17.6[a]
S5	25	>80	>80	>80	>80	>80	**S5m**	<4[b]

[a] After first cycle, polymer no longer soluble in aqueous solutions. [b] Not soluble in aqueous solutions.

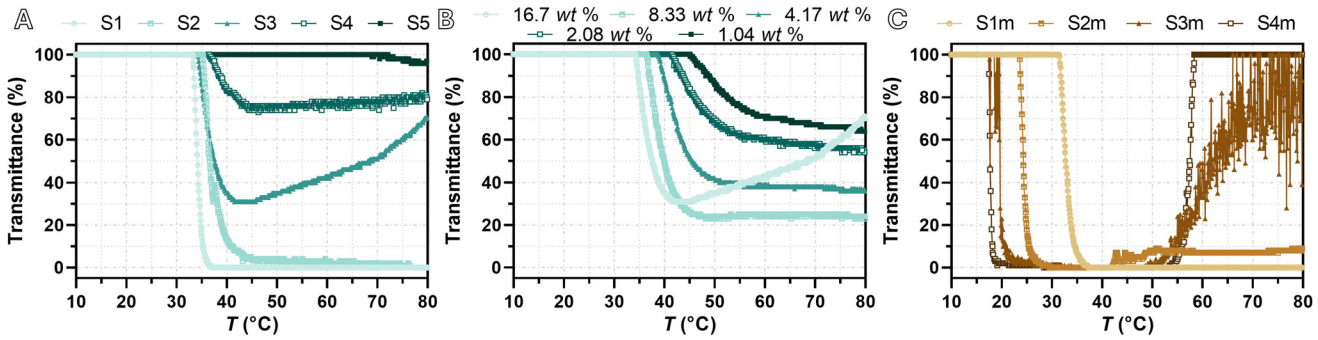

Fig. 6 Turbidimetry of the polymer solutions, with the methylated variants denoted by "m", as a function of temperature (10 to 80 °C) of (A) all samples at the highest polymer concentrations (16.7 wt% in 140 mM PBS, pH 7.4), (B) representative sample **S3** at 5 different polymer concentrations (1.04 to 16.7 wt% in 140 mM PBS, pH 7.4), and (C) all PMAATIPA-containing samples at a concentration of 1.04 wt% (140 mM PBS, pH 7.4). The drop in transmittance below 90% was regarded the T_{CP}. Upon further heating, the transmittance increased again in some samples, as the polymer phase coalesced and behaved unpredictably—sometimes remaining in the photon path, sometimes aggregated to the walls of the vial, thereby clearing the way of the photons.

tered polymers can greatly tune their local dissolution times. These results demonstrate that AATIPA is a highly hydrophilic monomer capable of tuning the thermoresponsiveness of thermoresponsive polymers. Additionally, carboxylic acid moieties of PAATIPA can be esterified after polymerization, thereby fine-tuning the polymers' hydrophilicity and thermoresponsiveness. These useful properties, along with its radiopacity, may pave the way for PAATIPA to be used in the future as constituting building block of smart polymers in biomedicine and clinical practice.

4.3. Detection limits of developed polymers

The radiopacity (RD) and detection limits of the synthesized polymers were assessed using micro-computed tomography (μCT) (Fig. 7). Average, minimal, and maximal RD values (RD_{aver}, RD_{min}, RD_{max}, respectively) for each sample are summarized in Tables S4 and S5.† All samples were clearly visible at high polymer concentrations (9.1 wt%, 100 mg mL^{-1}), exhibiting average RD values ranging from 88 to 1548 Hounsfield units (HU). For comparison, phosphate-buffered saline (PBS) was measured as a negative control (RD_{aver} = 1.1 ± 168 HU; RD_{min} = −299 HU; RD_{max} = 399 HU, Table S4†). Notably, a greater difference in radiopacity between the target object and the surrounding tissue allows for the detection of smaller volumes. For example, increasing the RD contrast from ≈50 to ≈1200 HU can reduce the minimum detectable hydrogel volume by over an order of magnitude.[24] Moreover, even higher contrast differences are generally required for reliable imaging *via* conventional X-ray radiography.[24]

When the resulting RDs of the samples are plotted as a function of the iodine concentration, the data exhibit a strong linear correlation (Fig. 7D and E). Linear regression yields comparable slopes for both polymer types (Table S6†), with coefficients of determination (R^2) around 0.98, indicating excellent fit quality. This demonstrates that the radiopacity of the polymer solutions increased linearly with iodine content, with an average increment of approximately 500 ± 40 Hounsfield units (HU) per 1 wt% of iodine. Based on previously published findings, radiodensities exceeding approximately 100–150 HU enable reliable detection of objects within soft tissues.

The detection limit of the polymers improved with increasing PAATIPA content, as observed by comparing **B3** with **B2** and **B1**, and with **B6**, as well as by the trend of increasing RD from **S1** to **S6**. Block copolymers **B2**, **B3**, **B5** and **B6** gave rise to detection limits around or below 0.6 wt%. Among the statistical copolymers, only **S4**, **S5** and **S6** showed sufficiently low detection limits (below 1.2 wt%) for practical imaging applications. Polymers **S5** and **S6**, which do not exhibit LCST behaviour and are fully water-soluble, may serve as promising carriers for the complexation and delivery of cationic peptides and proteins (see section 4.1.3). In contrast, **S4**—displaying LCST behaviour in both its carboxymethylated and carboxylate forms—could function as an injectable polymeric material with radiopaque properties.

4.4. pK_a of the PAATIPA homopolymer

To evaluate the acidity of PAATIPA, the homopolymer was synthesized *via* RAFT polymerization and characterized using two SEC methods to determine its degree of polymerization (DP), molar mass distribution, and polydispersity index (Table S3†). The purity and structure were confirmed *via* 1D and 2D ^{1}H NMR spectroscopy (Fig. S1–S3†). The acid dissociation constant (pK_a) of the resulting polymer was determined to be ≈2.3 (Fig. S119†), a value consistent with that of isophthalic acid (pK_{a1} = 2.24, pK_{a2} = 3.47 (ref. 49 and 50)). This low pK_a implies that at physiological pH (≈7.4), PAATIPA exists exclusively in its anionic form. This property significantly broadens the applicability of the developed block and statistical copolymers, as already evidenced by their high encapsulation efficiency for cationic rhodamine 6G and potential for loading other cationic APIs and biomolecules.

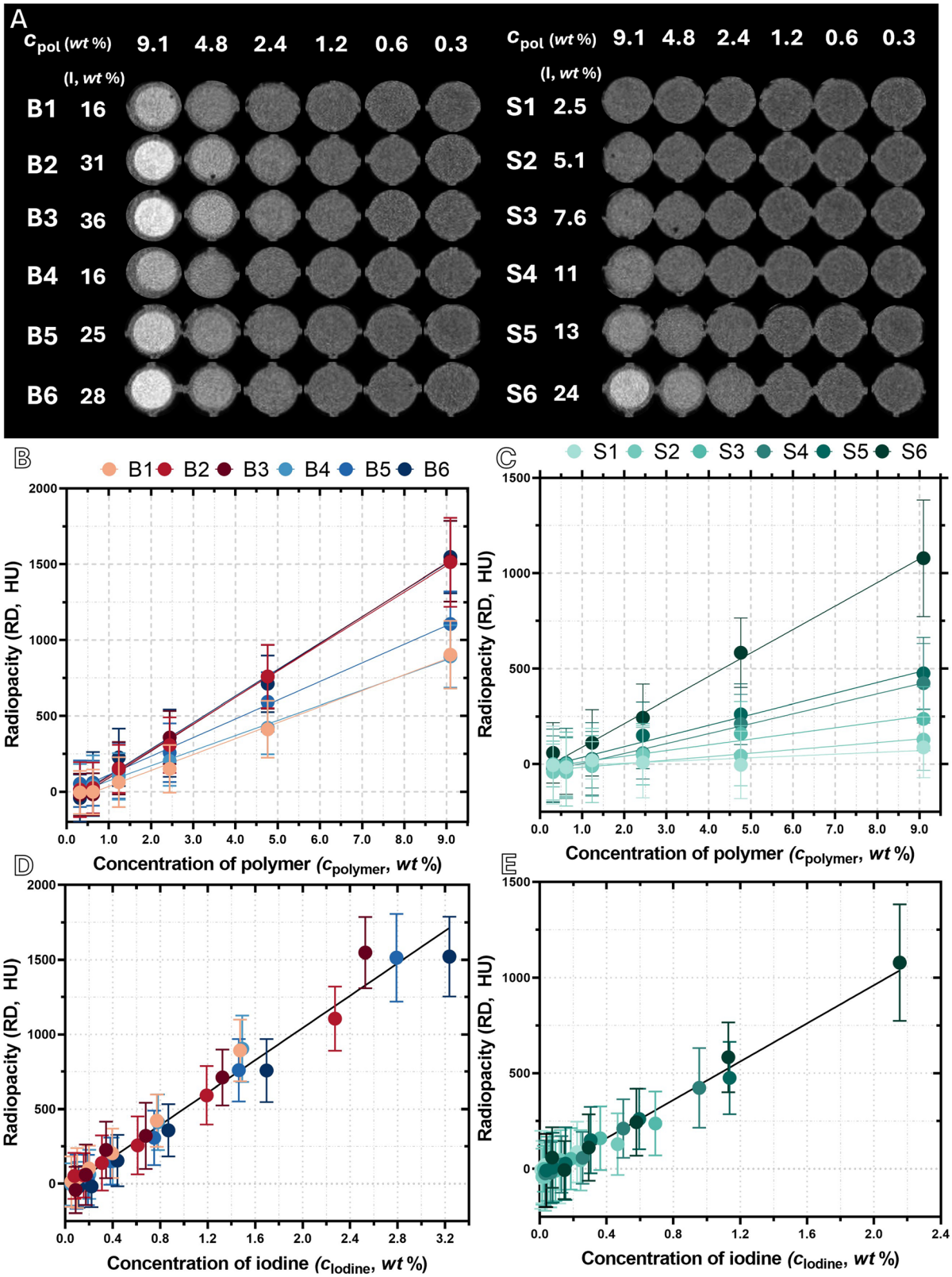

Fig. 7 (A) μCT images were acquired with preclinical X-CUBE micro-CT system (MOLECUBES; Ghent, Belgium), in "General-purpose mode" as previously described.[38] The solutions were prepared by 2-fold dilution of the first polymer concentration (100 mg mL^{-1} in 140 mM PBS, pH 7.4). The solutions were placed in a 96-well plate. The c_{pol} (wt%) is the polymer concentration in the specific sample; *I* (wt%) is the iodine content in the dry polymer. (B and C) The average RD and respective standard deviations plotted as a function of polymer concentration (wt%). (D and E) The average RD and respective standard deviations were plotted as a function of iodine concentration (wt%). Data were processed and fitted with a linear function in GraphPad Prism version 8.4.3. The RD values and respective standard deviations were obtained with AMIDE 1.0.6 using ellipsoidal ROIs.

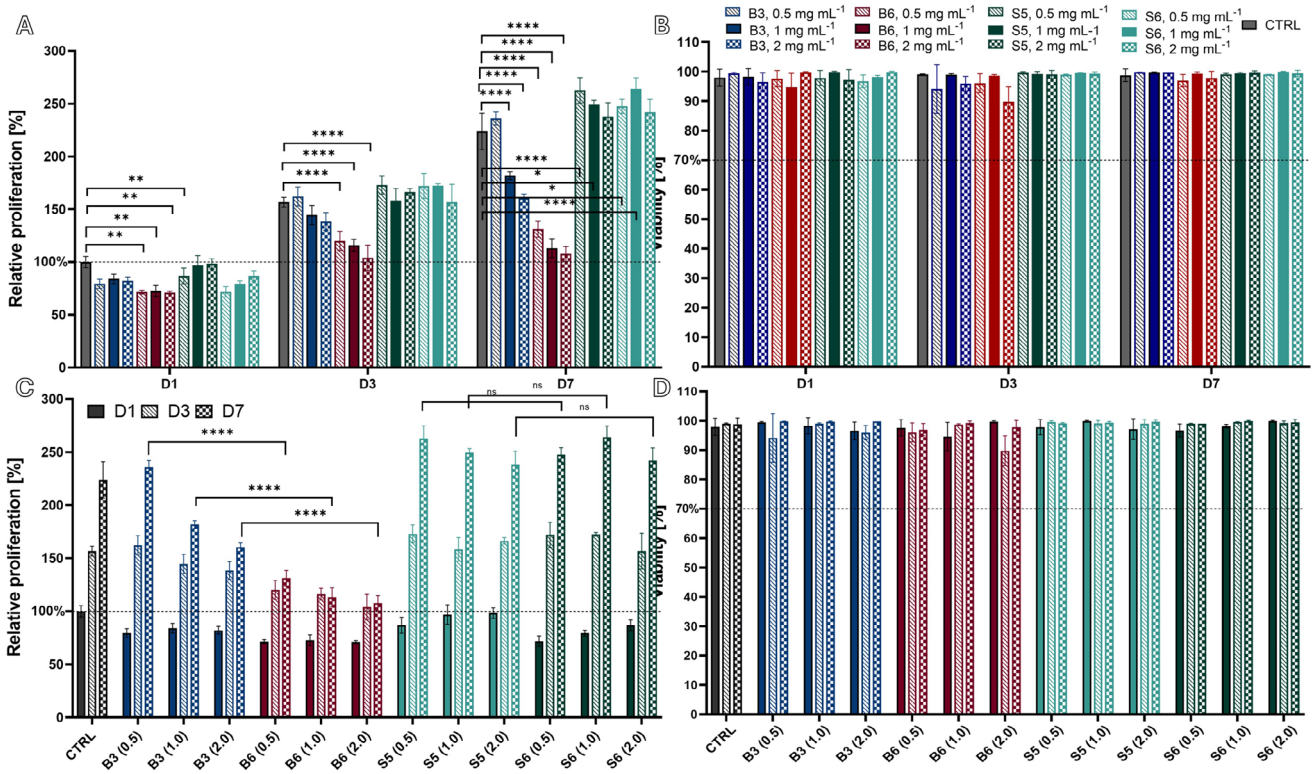

Fig. 8 Cytocompatibility evaluation of PAATIPA-containing polymer formulations using viability and metabolic activity assays. (A) Metabolic activity and (B) viability of HFFs compared across different time points. (C) Metabolic activity and (D) viability of HFFs compared across different polymer formulations. Metabolic activity values are normalized to the control. All experiments were performed in triplicate (N = 3) and statistical analysis was conducted using one-way ANOVA in GraphPad Prism version 8.4.3. Asterisks indicate levels of statistical significance: $p < 0.05$ (*), $p < 0.01$ (**), $p < 0.001$ (***), and $p < 0.0001$ (****); "ns" indicates no significant difference. For more detailed data analysis, see section S8 in ESI.†

Additionally, carboxylates derived from isophthalic acid are widely employed as intermediates in synthetic chemistry. As demonstrated by the straightforward methylation of the PAATIPA carboxylic acids, these functional groups offer a platform for further modification.[49] For instance, they could be derivatized to form esters with APIs, enabling controlled release systems (*via* slow hydrolysis), or used for covalent crosslinking to generate hydrogels.[49] Such hydrogels, bearing anionic functional groups, are expected to exhibit enhanced swelling behaviour—similar to poly(acrylic acid) (PAA)-based hydrogels[51]—and may also display antibacterial and antifouling properties, expanding their potential in biomedical applications.[52]

4.5. Cytotoxicity

As previously described, anionic polymers can exhibit antifouling and antimicrobial properties.[53] However, they may also induce cytotoxic effects, often as a result of their interactions with serum proteins.[54] Various strategies have been proposed to mitigate these effects in charged polymers, including the incorporation of neutral, hydrophobic, hydrophilic or counter-ion-containing monomers.[55] Therefore, the combination of PAATIPA with PNIPAM is expected to yield polymers with improved biocompatibility, as demonstrated in the following cytocompatibility study. The cytocompatibility of the PAATIPA-containing polymer formulations was evaluated using MTS and Live/Dead (L/D) assays over 7 days of direct culture with human foreskin fibroblasts (HFFs) (Fig. 8). The MTS assay revealed that the metabolic activity was influenced by both the polymer architecture and the AATIPA incorporation level, but all tested materials supported sustained cell proliferation. MTS assay results demonstrated that both time and material composition significantly influenced HFF proliferation (two-way ANOVA, $p < 0.001$ for time, condition, and interaction). As expected, cell metabolic activity increased over time across all conditions.

Among the statistical copolymers (PNIPAM-*s*-PAATIPA; **S5** and **S6**), both supported comparably high metabolic activity throughout the culture period. Notably, **S6**, synthesized with the highest AATIPA content (38.7 wt%), did not show reduced performance compared to **S5** (19.4 wt% PAATIPA). This suggests that the statistical copolymer architecture may localize PAATIPA moieties in a manner that limits direct interaction with cells, thereby reducing potential cytotoxic effects and preserving cell compatibility, even at higher AATIPA concentrations. In contrast, the block copolymers (PNIPAM-*b*-PAATIPA; **B3** and **B6**), where PAATIPA is concentrated in a separate block, exhibited slightly lower metabolic activity than the

statistical analogues. Interestingly, **B3**, which contains a higher PAATIPA weight fraction (58.2 wt%), showed less reduction in metabolic activity compared to **B6** (45.4 wt% PAATIPA). However, the number-average molar mass (M_n) of the PAATIPA block in **B6** (24.8 kDa) is significantly higher than that in **B3** (18.6 kDa), suggesting that it is not the PAATIPA content *per se*, but rather the length of the purely anionic PAATIPA block. However, rather than indicating cytotoxicity, this modest decline in metabolic activity is more likely reflective of cells reaching confluence or entering a slower growth phase by day 7.

Consistently, L/D staining confirmed high viability (>85%) for all polymer conditions, including the statistical copolymers, across all timepoints. This places all tested formulations well above the 70% viability threshold defined by ISO 10993-5:2009 for cytocompatibility. The L/D images can be found in Fig. S112–S115.† Even in the presence of high PAATIPA content or statistical incorporation, cells remained viable and well-adhered, reinforcing the conclusion that polymer structure – especially block *versus* statistical presentation – modulates proliferation dynamics without inducing cytotoxicity. The observed reduction in metabolic activity may therefore reflect a transient cellular stress response or altered proliferation, rather than cytotoxicity, as supported by the maintained membrane integrity in the live/dead assay. Interestingly, certain anionic polymers have been reported to induce so-called "cell cycle arrest" by interacting with components such as the anaphase-promoting complex/cyclosome (APC/C), without triggering cell death.[56,57] While this may provide a plausible explanation for the lower MTS readout in the presence of PNIPAM-*b*-PAATIPA, it remains speculative at this stage and warrants further investigation.

5. Conclusion

This study demonstrated the successful synthesis of PAATIPA-based block and statistical copolymers with promising applications in image-guided drug delivery, a key area within theranostics. The incorporation of PAATIPA imparted radiopacity, enabling non-invasive *in vivo* monitoring, while the thermoresponsive nature of PNIPAM facilitates self-assembly into nanoparticles for controlled drug delivery. The block copolymers formed nanosized particles, while statistical copolymers exhibited LCST behavior, with additional tunability achievable through methylation of PAATIPA's carboxylic groups. The anionic character of PAATIPA enhanced the encapsulation of cationic drugs, as demonstrated with rhodamine 6G compared to a PEG-containing reference polymer. Furthermore, the pK_a of PAATIPA ensured its stability at physiological pH, expanding its potential for diverse biomedical applications. The versatility of PAATIPA-based copolymers, combined with their low cytotoxicity, opens new avenues for controlled release systems and tissue engineering.

We demonstrated a linear increase in radiopacity of polymer solutions with increasing iodine content. For reliable detection of soft tissue contrast, an iodine content of approximately 0.3–0.4 wt% in solution was necessary to achieve radiodensity values in the range of 100–150 Hounsfield Units (HU). For the synthesized block copolymers, this threshold was reached at polymer concentrations of approximately 1.2–2.5 wt%, corresponding to a minimum of 26 wt% AATIPA in the polymer backbone (initiated from a 37 wt% AATIPA feed). In the case of statistical copolymers, similar radiopacity was obtained when the copolymer contained at least ~19 wt% AATIPA (from a 25 wt% AATIPA feed). These results underscore the importance of controlling the AATIPA content—and thus the iodine content—as well as the polymer concentration, regardless of the polymer architecture, which collectively determine the imaging efficiency and applicability of the contrast agents.

Conflicts of interest

The authors declare no conflicts of interest.

Data availability

The data supporting this article have been included as part of the ESI.† Additional raw data for this article, including GraphPad Prism files, OriginLab files, MestReNova NMR data, all images related to cytotoxicity study, .dcm and .xif files related to micro-CT data are available at Open Science Framework at **https://osf.io/td6pn/?view_only=25249ac9faa64d83a14f0c6f1bcabf89**.

Acknowledgements

N. Pien would like to acknowledge the financial support of the Research Foundation Flanders (FWO) under the form of an FWO junior post-doctoral research grant (12E4523N). K. K. gratefully acknowledges the financial support provided by Research Foundation – Flanders (FWO, Fonds Wetenschappelijk Onderzoek – Vlaanderen, project no. 1229422N and 1247425N). M. H. and Z. C. thank the Ministry of Health of the Czech Republic (grant # NW24-03-00387) and the Ministry of Education, Youth and Sports of the Czech Republic (grant # LUAUS24203). The study was co-funded by project New Technologies for Translational Research in Pharmaceutical Sciences/NETPHARM, project ID CZ.02.01.01/00/22_008/0004607, co-funded by the European Union. FNC gratefully acknowledges the support of the Research Foundation Flanders (FWO, G075621N & 1SC1225N). OG and KK gratefully acknowledge the co-funding of this project from the Grant Agency of Charles University (GA UK), project No. 199125. JVM gratefully acknowledge the support of the Research Foundation Flanders (FWO, 1SH7424N). The co-authors would like to thank Margot Haelterman for providing the reference polymer.

References

1 R. Singh, A. K. Mishra, B. Bhushan, H. Rawat and V. Kumar, A Glance on Gold Nanoparticle: An Emerging Theranostic Tool for Oncology, *J. Drug Delivery Sci. Technol.*, 2024, **97**, 105766, DOI: **10.1016/j.jddst.2024.105766**.

2 B. J. Burkett, D. J. Bartlett, P. W. McGarrah, A. R. Lewis, D. R. Johnson, K. Berberoğlu, M. K. Pandey, A. T. Packard, T. R. Halfdanarson, C. B. Hruska, G. B. Johnson and A. T. Kendi, A Review of Theranostics: Perspectives on Emerging Approaches and Clinical Advancements, *Radiol. Imaging Cancer*, 2023, **5**(4), e220157, DOI: **10.1148/rycan.220157**.

3 Z. Zhang, F.-L. Zhou, G.-L. Davies and G. R. Williams, Theranostics for MRI-Guided Therapy: Recent Developments, *VIEW*, 2022, **3**(3), 20200134, DOI: **10.1002/VIW.20200134**.

4 S. Tehrani Fateh, L. Moradi, E. Kohan, M. R. Hamblin and A. Shiralizadeh Dezfuli, Comprehensive Review on Ultrasound-Responsive Theranostic Nanomaterials: Mechanisms, Structures and Medical Applications, *Beilstein J. Nanotechnol.*, 2021, **12**, 808–862, DOI: **10.3762/bjnano.12.64**.

5 P. Cheng and K. Pu, Molecular Imaging and Disease Theranostics with Renal-Clearable Optical Agents, *Nat. Rev. Mater.*, 2021, **6**(12), 1095–1113, DOI: **10.1038/s41578-021-00328-6**.

6 Y. Jeong, H. S. Hwang and K. Na, Theranostics and Contrast Agents for Magnetic Resonance Imaging, *Biomater. Res.*, 2025, **22**(1), 20, DOI: **10.1186/s40824-018-0130-1**.

7 R. Vakili-Ghartavol, A. A. Momtazi-Borojeni, Z. Vakili-Ghartavol, H. T. Aiyelabegan, M. R. Jaafari, S. M. Rezayat and S. Arbabi Bidgoli, Toxicity Assessment of Superparamagnetic Iron Oxide Nanoparticles in Different Tissues, *Artif. Cells, Nanomed., Biotechnol.*, 2020, **48**(1), 443–451, DOI: **10.1080/21691401.2019.1709855**.

8 J. Ramalho, R. C. Semelka, M. Ramalho, R. H. Nunes, M. AlObaidy and M. Castillo, Gadolinium-Based Contrast Agent Accumulation and Toxicity: An Update, *AJNR Am. J. Neuroradiol.*, 2016, **37**(7), 1192, DOI: **10.3174/ajnr.A4615**.

9 J. Ruiz-Cabello, B. P. Barnett, P. A. Bottomley and J. W. M. Bulte, Fluorine (19F) MRS and MRI in Biomedicine, *NMR Biomed.*, 2011, **24**(2), 114–129, DOI: **10.1002/nbm.1570**.

10 D. Jirak, A. Galisova, K. Kolouchova, D. Babuka and M. Hruby, Fluorine Polymer Probes for Magnetic Resonance Imaging: Quo Vadis?, *MAGMA*, 2019, **32**(1), 173–185, DOI: **10.1007/s10334-018-0724-6**.

11 K. Kolouchova, O. Sedlacek, D. Jirak, D. Babuka, J. Blahut, J. Kotek, M. Vit, J. Trousil, R. Konefał, O. Janouskova, B. Podhorska, M. Slouf and M. Hruby, Self-Assembled Thermoresponsive Polymeric Nanogels for 19F MR Imaging, *Biomacromolecules*, 2018, **19**(8), 3515–3524, DOI: **10.1021/acs.biomac.8b00812**.

12 P. Švec, O. V. Petrov, J. Lang, P. Štěpnička, O. Groborz, D. Dunlop, J. Blahut, K. Kolouchová, L. Loukotová, O. Sedláček, T. Heizer, Z. Tošner, M. Šlouf, H. Beneš, R. Hoogenboom and M. Hrubý, Fluorinated Ferrocene Moieties as a Platform for Redox-Responsive Polymer 19F MRI Theranostics, *Macromolecules*, 2022, **55**(2), 658–671, DOI: **10.1021/acs.macromol.1c01723**.

13 U. Sharma, E. W. Chang and S. H. Yun, Long-Wavelength Optical Coherence Tomography at 1.7 Mm for Enhanced Imaging Depth, *Opt. Express*, 2008, **16**(24), 19712–19723, DOI: **10.1364/OE.16.019712**.

14 G. Yang, J. Liu, Y. Wu, L. Feng and Z. Liu, Near-Infrared-Light Responsive Nanoscale Drug Delivery Systems for Cancer Treatment, *Coord. Chem. Rev.*, 2016, **320–321**, 100–117, DOI: **10.1016/j.ccr.2016.04.004**.

15 S. Mattsson and M. Söderberg, Radiation Dose Management in CT, SPECT/CT and PET/CT Techniques, *Radiat. Prot. Dosim.*, 2011, **147**(1–2), 13–21, DOI: **10.1093/rpd/ncr261**.

16 M. A. Wheatley and J. R. Eisenbrey, 9.27 - Polymeric Imaging Agents, in *Polymer Science: A Comprehensive Reference*, ed. K. Matyjaszewski and M. Möller, Elsevier: Amsterdam, 2012, pp. 529–545. DOI: **10.1016/B978-0-444-53349-4.00232-6**.

17 N. Elahi, M. Kamali and M. H. Baghersad, Recent Biomedical Applications of Gold Nanoparticles: A Review, *Talanta*, 2018, **184**, 537–556, DOI: **10.1016/j.talanta.2018.02.088**.

18 A. Sani, C. Cao and D. Cui, Toxicity of Gold Nanoparticles (AuNPs): A Review, *Biochem. Biophys. Rep.*, 2021, **26**, 100991, DOI: **10.1016/j.bbrep.2021.100991**.

19 Q.-Y. Cai, S. H. Kim, K. S. Choi, S. Y. Kim, S. J. Byun, K. W. Kim, S. H. Park, S. K. Juhng and K.-H. Yoon, Colloidal Gold Nanoparticles as a Blood-Pool Contrast Agent for X-Ray Computed Tomography in Mice, *Invest. Radiol.*, 2007, **42**(12), 797–806, DOI: **10.1097/RLI.0b013e31811ecdcd**.

20 O. Rabin, J. Manuel Perez, J. Grimm, G. Wojtkiewicz and R. Weissleder, An X-Ray Computed Tomography Imaging Agent Based on Long-Circulating Bismuth Sulphide Nanoparticles, *Nat. Mater.*, 2006, **5**(2), 118–122, DOI: **10.1038/nmat1571**.

21 A. Sachse, Iodinated Liposomes as Contrast Agents, in *Nanoparticles in Biomedical Imaging: Emerging Technologies and Applications*, ed. J. W. M. Bulte and M. M. J. Modo, Springer New York, New York, NY, 2008, pp. 371–410. DOI: **10.1007/978-0-387-72027-2_18**.

22 A. Galperin, D. Margel, J. Baniel, G. Dank, H. Biton and S. Margel, Radiopaque Iodinated Polymeric Nanoparticles for X-Ray Imaging Applications, *Biomaterials*, 2007, **28**(30), 4461–4468, DOI: **10.1016/j.biomaterials.2007.06.032**.

23 D. Horák, M. Metalová and F. Rypáček, New Radiopaque PolyHEMA-Based Hydrogel Particles, *J. Biomed. Mater. Res.*, 1997, **34**(2), 183–188, DOI: **10.1002/(SICI)1097-4636(199702)34:2<183::AID-JBM7>3.0.CO;2-M**.

24 O. Groborz, K. Kolouchova, L. Parmentier, A. Szabo, B. Van Durme, D. Dunlop, T. Slanina and S. Van Vlierberghe, Photoprintable Radiopaque Hydrogels for Regenerative

Medicine, *ACS Appl. Eng. Mater.*, 2024, **2**(4), 811–817, DOI: **10.1021/acsaenm.3c00533**.

25 K. Kolouchova, Q. Thijssen, O. Groborz, L. Van Damme, J. Humajova, P. Matous, A. Quaak, M. Dusa, J. Kucka, L. Sefc, M. Hruby and S. Van Vlierberghe, Next-Gen Poly(ε-Caprolactone) Scaffolds: Non-Destructive In Vivo Monitoring and Accelerated Biodegradation, *Adv. Healthc. Mater.*, 2025, **14**(1), 2402256, DOI: **10.1002/adhm.202402256**.

26 I. J. Das and T. Bal, PH Factors in Chronic Wound and PH-Responsive Polysaccharide-Based Hydrogel Dressings, *Int. J. Biol. Macromol.*, 2024, **279**, 135118, DOI: **10.1016/j.ijbiomac.2024.135118**.

27 O. S. Fenton, K. N. Olafson, P. S. Pillai, M. J. Mitchell and R. Langer, Advances in Biomaterials for Drug Delivery, *Adv. Mater.*, 2018, **30**(29), 1705328, DOI: **10.1002/adma.201705328**.

28 G. Zhang, X. Zeng and P. Li, Nanomaterials in Cancer-Therapy Drug Delivery System, *J. Biomed. Nanotechnol.*, 2013, **9**, 741–750, DOI: **10.1166/jbn.2013.1583**.

29 S. Bamrungsap, Z. Zhao, T. Chen, L. Wang, C. Li, T. Fu and W. Tan, Nanotechnology in Therapeutics: A Focus on Nanoparticles as a Drug Delivery System, *Nanomedicine*, 2012, **7**(8), 1253–1271, DOI: **10.2217/nnm.12.87**.

30 S. Ganta, H. Devalapally, A. Shahiwala and M. Amiji, A Review of Stimuli-Responsive Nanocarriers for Drug and Gene Delivery, *J. Controlled Release*, 2008, **126**(3), 187–204, DOI: **10.1016/j.jconrel.2007.12.017**.

31 M. Srinivas, P. Boehm-Sturm, C. G. Figdor, I. J. de Vries and M. Hoehn, Labeling Cells for in Vivo Tracking Using 19F MRI, *Biomaterials*, 2012, **33**(34), 8830–8840, DOI: **10.1016/j.biomaterials.2012.08.048**.

32 A. Servant, I. Jacobs, C. Bussy, C. Fabbro, T. da Ros, E. Pach, B. Ballesteros, M. Prato, K. Nicolay and K. Kostarelos, Gadolinium-Functionalised Multi-Walled Carbon Nanotubes as a T1 Contrast Agent for MRI Cell Labelling and Tracking, *Carbon*, 2016, **97**, 126–133, DOI: **10.1016/j.carbon.2015.08.051**.

33 K. Kolouchova, D. Jirak, O. Groborz, O. Sedlacek, N. Ziolkowska, M. Vit, E. Sticova, A. Galisova, P. Svec, J. Trousil, M. Hajek and M. Hruby, Implant-Forming Polymeric 19F MRI-Tracer with Tunable Dissolution, *J. Controlled Release*, 2020, **327**, 50–60, DOI: **10.1016/j.jconrel.2020.07.026**.

34 O. Groborz, K. Kolouchová, J. Pankrác, P. Keša, J. Kadlec, T. Krunclová, A. Pierzynová, J. Šrámek, M. Hovořáková, L. Dalecká, Z. Pavlíková, P. Matouš, P. Páral, L. Loukotová, P. Švec, H. Beneš, L. Štěpánek, D. Dunlop, C. V. Melo, L. Šefc, T. Slanina, J. Beneš, S. Van Vlierberghe, R. Hoogenboom and M. Hrubý, Pharmacokinetics of Intramuscularly Administered Thermoresponsive Polymers, *Adv. Healthc. Mater.*, 2022, **11**(22), 2201344, DOI: **10.1002/adhm.202201344**.

35 K. Kolouchova, O. Groborz, M. Slouf, V. Herynek, L. Parmentier, D. Babuka, Z. Cernochova, F. Koucky, O. Sedlacek, M. Hruby, R. Hoogenboom and S. Van Vlierberghe, Thermoresponsive, Triblock Copolymers as Widely Applicable 19F Magnetic Resonance Imaging Tracers, *Chem. Mater.*, 2022, **34**(24), 10902–10916, DOI: **10.1021/acs.chemmater.2c02589**.

36 J. Jakeš, Regularized Positive Exponential Sum (REPES) Program - A Way of Inverting Laplace Transform Data Obtained by Dynamic Light Scattering, *Collect. Czech. Chem. Commun.*, 1995, **60**(11), 1781–1797.

37 M. Štěpánek, J. Hajduová, K. Procházka, M. Šlouf, J. Nebesářová, G. Mountrichas, C. Mantzaridis and S. Pispas, Association of Poly(4-Hydroxystyrene)-Block-Poly (Ethylene Oxide) in Aqueous Solutions: Block Copolymer Nanoparticles with Intermixed Blocks, *Langmuir*, 2012, **28**(1), 307–313, DOI: **10.1021/la203946s**.

38 F. M. Muller, C. Vanhove, B. Vandeghinste and S. Vandenberghe, Performance Evaluation of a Micro-CT System for Laboratory Animal Imaging with Iterative Reconstruction Capabilities, *Med. Phys.*, 2022, **49**(5), 3121–3133, DOI: **10.1002/mp.15538**.

39 P. Zhang, F. Sun, S. Liu and S. Jiang, Anti-PEG Antibodies in the Clinic: Current Issues and beyond PEGylation, *J. Controlled Release*, 2016, **244**, 184–193, DOI: **10.1016/j.jconrel.2016.06.040**.

40 P. Bigini, M. Gobbi, M. Bonati, A. Clavenna, M. Zucchetti, S. Garattini and G. Pasut, The Role and Impact of Polyethylene Glycol on Anaphylactic Reactions to COVID-19 Nano-Vaccines, *Nat. Nanotechnol.*, 2021, **16**(11), 1169–1171, DOI: **10.1038/s41565-021-01001-3**.

41 X. Yao, C. Qi, C. Sun, F. Huo and X. Jiang, Poly(Ethylene Glycol) Alternatives in Biomedical Applications, *Nano Today*, 2023, **48**, 101738, DOI: **10.1016/j.nantod.2022.101738**.

42 F. Chen, E. B. Ehlerding and W. Cai, Theranostic Nanoparticles., *J. Nucl. Med.*, 2014, **55**(12), 1919–1922, DOI: **10.2967/jnumed.114.146019**.

43 S.-J. Park and M.-K. Seo, Chapter 1 - Intermolecular Force, in *Interface Science and Technology*, ed. S.-J. Park and M.-K. Seo, Elsevier, 2011, vol. 18, pp. 1–57. DOI: **10.1016/B978-0-12-375049-5.00001-3**.

44 V. Ow, Q. Lin, J. H. M. Wong, B. Sim, Y. L. Tan, Y. Leow, R. Goh and X. J. Loh, Understanding the Interplay between PH and Charges for Theranostic Nanomaterials, *Nanoscale*, 2025, **17**(12), 6960–6980, DOI: **10.1039/D4NR03706E**.

45 N. Ahmed, H. Fessi and A. Elaissari, Theranostic Applications of Nanoparticles in Cancer, *Drug Discovery Today*, 2012, **17**(17–18), 928–934, DOI: **10.1016/j.drudis.2012.03.010**.

46 L. Zhang, F. X. Gu, J. M. Chan, A. Z. Wang, R. S. Langer and O. C. Farokhzad, Nanoparticles in Medicine: Therapeutic Applications and Developments, *Clin. Pharmacol. Ther.*, 2008, **83**(5), 761–769, DOI: **10.1038/sj.clpt.6100400**.

47 P. Pallavi, K. Girigoswami, P. Gowtham, K. Harini, A. Thirumalai and A. Girigoswami, Encapsulating Rhodamine 6G in Oxidized Sodium Alginate Polymeric Hydrogel for Photodynamically Inactivating Cancer Cells, *Curr. Pharm. Des.*, 2024, **30**(35), 2801–2812, DOI: **10.2174/0113816128307606240722072006**.

48 A. S. Hoffman, P. S. Stayton, V. Bulmus, G. Chen, J. Chen, C. Cheung, A. Chilkoti, Z. Ding, L. Dong, R. Fong,

C. A. Lackey, C. J. Long, M. Miura, J. E. Morris, N. Murthy, Y. Nabeshima, T. G. Park, O. W. Press, T. Shimoboji, S. Shoemaker, H. J. Yang, N. Monji, R. C. Nowinski, C. A. Cole, J. H. Priest, J. M. Harris, K. Nakamae, T. Nishino and T. Miyata, Really Smart Bioconjugates of Smart Polymers and Receptor Proteins, *J. Biomed. Mater. Res.*, 2000, **52**(4), 577–586, DOI: **10.1002/1097-4636(20001215)52:4<577::AID-JBM1>3.0.CO;2-5**.

49 P. M. Lorz, F. K. Towae, W. Enke, R. Jäckh, N. Bhargava and W. Hillesheim, Phthalic Acid and Derivatives, in *Ullmann's Encyclopedia of Industrial Chemistry*, 2007. DOI: **10.1002/14356007.a20_181.pub2**.

50 P. Jafari, M. Barzegar-Jalali, S. Hemmati and A. Jouyban, Determination of the Solubility Profile of Isophthalic Acid in Some Aqueous Solutions of Betaine-Based Deep Eutectic Solvents: Study the Extent of H-Bonding Interactions between Starting Materials of Deep Eutectic Solvents in Aqueous Medium, *Sustainable Chem. Pharm.*, 2023, **35**, 101208, DOI: **10.1016/j.scp.2023.101208**.

51 W. Feng and Z. Wang, Tailoring the Swelling-Shrinkable Behavior of Hydrogels for Biomedical Applications, *Adv. Sci.*, 2023, **10**(28), 2303326, DOI: **10.1002/advs.202303326**.

52 M. Haktaniyan and M. Bradley, Polymers Showing Intrinsic Antimicrobial Activity, *Chem. Soc. Rev.*, 2022, **51**(20), 8584–8611, DOI: **10.1039/D2CS00558A**.

53 F. Yang, H. Liu, Y. Wei, R. Xue, Z. Liu, X. Chu, X. Tian, L. Yin and H. Tang, Antibacterial Brush Polypeptide Coatings with Anionic Backbones, *Acta Biomater.*, 2023, **155**, 359–369, DOI: **10.1016/j.actbio.2022.11.020**.

54 F. Richter, K. Leer, L. Martin, P. Mapfumo, J. I. Solomun, M. T. Kuchenbrod, S. Hoeppener, J. C. Brendel and A. Traeger, The Impact of Anionic Polymers on Gene Delivery: How Composition and Assembly Help Evading the Toxicity-Efficiency Dilemma, *J. Nanobiotechnol.*, 2021, **19**(1), 292, DOI: **10.1186/s12951-021-00994-2**.

55 A. M. Weiss, M. A. I. I. Lopez, B. W. Rawe, S. Manna, Q. Chen, E. J. Mulder, S. J. Rowan and A. P. Esser-Kahn, Understanding How Cationic Polymers' Properties Inform Toxic or Immunogenic Responses via Parametric Analysis, *Macromolecules*, 2023, **56**(18), 7286–7299, DOI: **10.1021/acs.macromol.3c01223**.

56 A. Mizrak and D. O. Morgan, Polyanions Provide Selective Control of APC/C Interactions with the Activator Subunit, *Nat. Commun.*, 2019, **10**(1), 5807, DOI: **10.1038/s41467-019-13864-1**.

57 T. Bodrug, K. A. Welsh, M. Hinkle, M. J. Emanuele and N. G. Brown, Intricate Regulatory Mechanisms of the Anaphase-Promoting Complex/Cyclosome and Its Role in Chromatin Regulation, *Front. Cell Dev. Biol.*, 2021, **9**, 1–18, DOI: **10.3389/fcell.2021.687515**.